

# Erasmus Mundus

European Master of Science in  
Nuclear Fusion and Engineering Physics

## **Beam Transmission Monitoring of the TJ-II Neutral Beam Injectors**

Master Thesis  
presented by

**Julius Damba**

Thesis Promoter  
José Ramón Martín Solís  
Universidad Carlos III de Madrid

Thesis Supervisor  
Macarena Liniers  
Laboratorio Nacional de Fusión (CIEMAT)

July 07th, 2014



# **Beam Transmission Monitoring of the TJ-II Neutral Beam Injectors**

Master Thesis  
presented by

**Julius Damba**

Thesis Promoter  
José Ramón Martín Solís  
Universidad Carlos III de Madrid

Thesis Supervisor  
Macarena Liniers  
Laboratorio Nacional de Fusión (CIEMAT)

Erasmus Mundus Program on Nuclear Fusion Science and  
Engineering Physics

July 07th, 2014





# Abstract

Neutral Beam Injection (NBI) is a widely used method for heating fusion plasmas. Since NBI heating efficiency is not dependent on magnetic configuration, it has been employed in all types of magnetic confinement devices (tokamaks, stellarators, Z-pinch). The NBI system at JET consists of two injection lines at 125 keV energy and total power 34 MW, that has allowed to reach 12 keV ion temperature.

Moreover, the use of NBI heating is fundamental for achieving the plasma parameters and  $Q$  factor ( $\geq 10$ ) required for a successful scientific programme for ITER (International Tokamak Experimental Reactor), that will use two beamlines of 1 MeV energy and 16 MW power. Last generation NBI systems are both complex and expensive, and their poor energy efficiency has raised questions about their use in DEMO - a future demonstration power plant. With present day technologies, only a fraction between 20–40 % of power reaches the plasma. Thus, if such systems are to be maintained, it is essential to employ the beam power generated as efficiently as possible.

The main power loss channels affecting NBI efficiency are the neutralization and transmission losses. Beams are transmitted through the apertures connecting the beamline and the confinement machine. Geometrical losses are associated to the unavoidable beam divergence: direct interception of the beam periphery by some wall areas gives rise to gas re-emission and the creation of a gas target for the loss-carrying re-ionization reactions. High geometrical and re-ionization losses are associated with narrow beam ducts.

In TJ-II, the Helic type stellarator at the Laboratorio Nacional de Fusión, at CIEMAT, two Neutral Beam Injectors of 0.7 MW power and 34 keV energy, are presently operated. In TJ-II, as in all stellarators, the pronounced helicity of the heliac configuration complicates beam access to the plasma, due to the narrow space available between two neighbouring toroidal field coils. NBI transmission optimization is necessary in order to deliver maximum power and fast particle current to the plasma, and to minimize beam interception by surfaces thereby reducing gas re-emission. To study the behaviour of NBI heated plasmas, it is necessary to have a correct knowledge of the beam power balance. In TJ-II, attainment of the high confinement mode ('H-mode') is the object of sustained effort in the latest campaigns, with particular attention being given to the beam power threshold. A series of experiments has been carried out at TJ-II tackling the effect of the NBI generated fast ions on the excitation of Alfvén eigenmodes. For the correct interpretation of the results,

the beam particle current corresponding to each set of beam parameters must be determined. It is highly desirable to develop the use of adequate experimental tools to obtain a good estimate of the transmitted power and current, within the unavoidable uncertainties.

In this study, beam transmission has been studied for a range of beam parameters corresponding to two different scans: a beam current scan (40 A to 60 A) at constant beam energy (31 keV), and a beam energy scan (25 keV to 33 keV) at constant beam current (52 A). In the scans, the beam perveance is varied together with beam power, and consequently the optical properties of the beam are changed. Also, the power losses due to re-ionization of the fast neutrals have been studied for the different beam parameters of the scan, since the reionization rate depends on beam energy (the cross section varies with energy) and on the gas target (gas re-emission depends on beam power). The transmission of the beam has been studied at three targets along the beam path:

- The V-calorimeter that intercepts the full beam upstream of the beam duct, allows to obtain the beam transmission and neutralization fraction. The dependence of transmission on perveance has been determined for the parameter scan of this study.
- The Target Calorimeter (TC) allows to obtain power density profiles of the beam at the duct exit, near the beam focus. From the Gaussian fits of the profiles, the beam angular divergence can be extracted. For the parameter scans in this study, the perveance value that leads to maximum transmission at the V-calorimeter, corresponds to minimum divergence and maximum temperature at the Target Calorimeter. In the current scan, horizontal profiles displayed divergence angles between  $1.2^\circ$  and  $1.35^\circ$ . In the energy scan a wider span of the divergence angle ( $1.2^\circ$  to  $1.7^\circ$ ) has been observed.
- Beam Stop: comparison of the target temperatures in shots with/without  $\vec{B}$ -field, yields an estimate of the re-ionization fraction. Re-ionization has been estimated for the same beam parameter scans as for the other targets. In the present experiments, large re-ionization fractions (25 %–35 %) in excess of the more usual values (15 %–20 %) have been found. A good correlation between re-ionization losses and residual gas pressure is found for the beam energy scans, but not for the current scans. Reionization profiles have been obtained at the BS target, showing a clear inhomogeneity of the re-ionization rate in the beam cross section. The NBI transmission study carried out for the Master Thesis work will be continued to calculate the power and particle current entering the plasma for the set of beam parameters in the scan, with a beam simulation code -DENSBB- that uses a complete 3D model for the duct and TJ-II vacuum vessel. The power and current values will be the necessary input for the plasma ‘H-mode’ and Alfvén eigenmode studies.

# Contents

<b>1</b>	<b>Introduction</b>	<b>5</b>
1.1	Fusion Energy . . . . .	5
1.1.1	Nuclear fusion power . . . . .	5
1.2	Magnetic confinement . . . . .	8
1.2.1	Tokamaks . . . . .	10
1.2.2	Stellarators . . . . .	11
1.3	Plasma heating . . . . .	13
1.3.1	Radio frequency (RF) heating . . . . .	13
1.3.2	Neutral beam injection (NBI) heating . . . . .	14
<b>2</b>	<b>NBI heating systems</b>	<b>15</b>
2.1	Neutral beam generation and transport . . . . .	15
2.1.1	Ion source . . . . .	15
2.1.2	Neutralizer . . . . .	17
2.1.3	Ion removal system (bending magnet (BM) and ion dump) . . . . .	17
2.1.4	Beamline Calorimeter . . . . .	17
2.1.5	Beam duct . . . . .	18
2.1.6	Primary vacuum system . . . . .	18
2.2	Beam transmission . . . . .	18
2.2.1	Neutralization losses . . . . .	18
2.2.2	Re-ionization losses . . . . .	19
2.2.3	Geometrical losses . . . . .	19
2.3	Motivation . . . . .	22
<b>3</b>	<b>Neutral Beam Injection at TJ-II</b>	<b>25</b>
3.1	The TJ-II stellarator . . . . .	25
3.2	The NBI system at TJ-II . . . . .	26
<b>4</b>	<b>Methodology and Diagnostic techniques</b>	<b>31</b>
4.1	The semi-infinite solid approximation . . . . .	31
4.2	Water calorimetry at the ‘V-calorimeter’ . . . . .	34
4.3	Infrared (IR) Thermography Principle . . . . .	38
4.4	IR Cameras . . . . .	39
4.5	The Target Calorimeter . . . . .	40
4.5.1	IR images as thermal prints of the beam . . . . .	40

4.5.2	Transformation from Image Coordinates to Real Coordinates . . . . .	43
4.5.3	Measurement of beam power density at two localized points on the Target . . . . .	45
4.6	The Beam Stop Target . . . . .	47
4.7	Fast Ion Gauge (FIG) . . . . .	49
<b>5</b>	<b>Results</b>	<b>53</b>
5.1	V-calorimeter . . . . .	53
5.2	Target Calorimeter (TC) . . . . .	57
5.3	Beam Stop (BS) . . . . .	61
<b>6</b>	<b>Discussion</b>	<b>67</b>
<b>7</b>	<b>Summary</b>	<b>69</b>
<b>8</b>	<b>Appendix</b>	<b>71</b>
8.1	Appendix 1 . . . . .	71

# Chapter 1

## Introduction

### 1.1 Fusion Energy

In this era of increased global climate change, humanity's long-term reliance on fossil fuels as a source of power may not be sustainable. The solution to this will therefore lie in the availability of alternative sources of energy. This includes nuclear power. Generating power from nuclear reactions involves splitting heavy atoms into lighter components in a controlled fashion (fission) or bringing light elements together to form a heavier one (fusion).

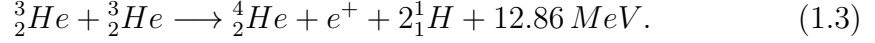
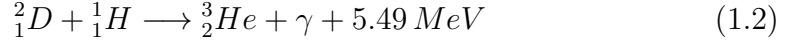
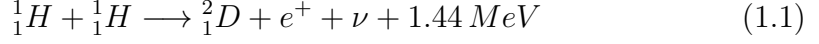
In both reactions, elements with higher binding energies are formed. Binding energy in the physical sense means negative potential energy, which implies an increase in kinetic energy. Nuclear fusion reactions are most readily initiated by light elements whereas fission reactions are most readily initiated by heavy elements.

Fusion energy liberated is therefore a result of the binding energy of nucleons, which is given by Einstein's energy relation  $E = mc^2$ . The mass of the resulting nucleus in a fusion reaction is less than the sum of the masses of the individual reactants' nuclei. This mass defect is therefore the source of very high amounts of energy released in a nuclear fusion reaction. For decades now, all the nuclear power plants have been based on fission. Fission, though safe with good regulations and strict safety rules, the fuel used is radioactive and waste disposal can be problematic. With the occurrence of such disasters as the Fukushima in March 2011, there is a high risk of accidents associated with fission. Nuclear fusion on the other hand, is in principle cleaner and comes from a cheaper and more abundant fuel source â deuterium, with only helium produced as waste. Deuterium is an isotope of hydrogen which can be extracted from sea water.

#### 1.1.1 Nuclear fusion power

The best known fusion reactors of all are the stars. Fusion is what powers stars like the Sun. In the core of the Sun, strong gravitational pressure forces together hydrogen plasma (an equal mixture of protons and electrons) at fifteen

(15) million degrees. These extreme conditions of temperature and pressure give protons enough energy to overcome their mutual repulsions. When protons fuse together they are converted into deuterons and release a lot of energy. The reactions that take place in the stars with relatively low central temperatures are described by the proton-proton cycle as shown [1]:



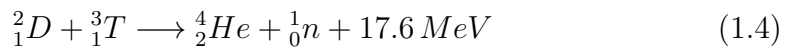
Here,  $e^+$ ,  $\gamma$  and  $\nu$  respectively denote positron, gamma ray, and neutrino. Fusion therefore provides an alternative way to liberate the energy of the nucleus by imitating the process powering the Sun and all the stars. The use of deuterium ( $D$ ) or tritium ( $T$ ), which are isotopes of hydrogen, instead of hydrogen has been preferred due to the lower energy requirements to start the fusion reaction.

To have nuclear fusion reactions in the laboratory, bombardment of a light nucleus by another light element is preferred. Deuterium ( $D$ ), Tritium ( $T$ ) and Helium-3 ( $He^3$ ) are the main elements that can be used. Therefore, the three main nuclear fusion reactions are Deuterium-Deuterium ( $D-D$ ), Deuterium-Helium-3 ( $D-He^3$ ), or Deuterium-Tritium ( $D-T$ ) reactions.  $D-D$  reaction is very difficult to initiate.  $D-He^3$  has the highest energy yield of the three reactions and the reaction products are charged particles which reduce activation and material damage. Its disadvantage relates to the difficulty in initiation of the reaction, and the  $He^3$  is not readily available. The  $D-T$  reaction scheme is the easiest to initiate and has a good energy yield, due to its high fusion cross section and reaction rate (see Fig. 1.1). The disadvantage of the  $D-T$  reaction scheme is the release of large number of neutrons in the process, which causes material activation. Also, the tritium used is radioactive with a half-life of 12.26 years and it is not naturally occurring.

The deuterium-tritium ( $D-T$ ) reaction (see Eq. 1.4) is the preferred fusion reaction scheme, since its probability to occur at relatively lower temperatures compared to the other reaction schemes is higher. This probability (for two nuclei to undergo a fusion reaction) is described by the fusion reaction cross section  $\sigma$ , which defines the fusion reaction rate term  $\langle \sigma v \rangle$ .  $v$  is the relative velocity of the colliding/fusing particles [2, 3].

Fig. 1.1 shows comparisons of the  $D-D$ ,  $D-T$  and  $D-He^3$  fusion reaction cross sections and reaction rates. The  $D-T$  reaction scheme has the largest cross section among the three schemes, which is achieved at relatively low energies and it has the highest reaction rate which occurs at  $\sim 70$  keV ion temperature.

The  $D-T$  reaction scheme is given by the equation



The energy released per reaction is 17.6 MeV, ( $\sim 10,000,000$  times more than the energy released in a typical chemical reaction). This energy is ap-

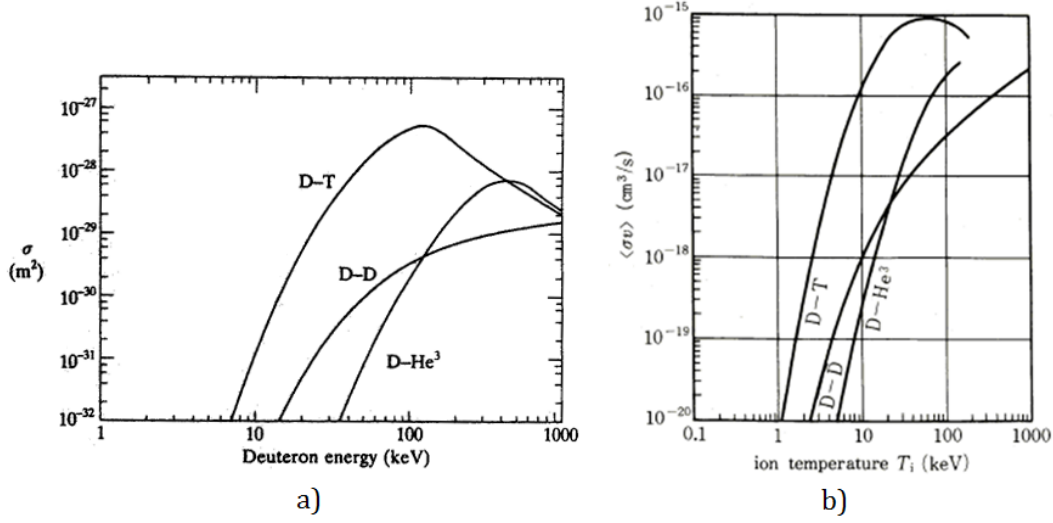


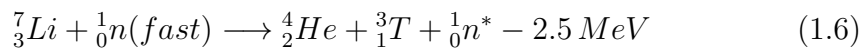
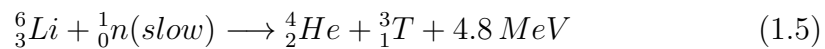
FIGURE 1.1: Fusion reaction cross section and rates for  $D-D$ ,  $D-T$  and  $D-He^3$  reaction schemes compared. a) Fusion cross sections dependence on the deuterium energy and b) Fusion reaction rates dependence on ion temperature, for the three nuclear fusion reaction schemes [2, 3].

portioned between the two end products, such that 3.5 MeV goes to  ${}^4_2\text{He}$  ( $\alpha$ -particles) and 14.1 MeV goes to the neutrons produced. In a reactor device, actual heating of the plasma is by the  $\alpha$ -particles. This means that in an optimal fuel mixture of  $D$  and  $T$  (with equal number densities  $n$  of  $D$  and  $T$ ), the fusion power density (fusion power per unit volume) that can be achieved,  $S_f$  is given by  $S_f = E \cdot n^2 \cdot \langle \sigma v \rangle / 4$  [1, 3].

The energetic neutrons escape from the plasma through the vacuum vessel, and are absorbed by a dense blanket material. The blanket material is designed to enable the thermal energy due the incident energetic neutrons to be converted into steam to drive turbines which are used for generating electricity. Thermalised neutrons in the blanket are further used for initiating and maintaining the breeding of tritium in the Lithium blanket. The reactor therefore, is capable of generating electric power while generating its own fuel in this process.

Fig. 1.2 shows the  $D-T$  reaction scheme.

Tritium breeding can be achieved by bombarding Lithium isotopes (lithium-6 ( ${}^6_3\text{Li}$ ) or Lithium-7 ( ${}^7_3\text{Li}$ )) with neutrons.  ${}^6_3\text{Li}$  bombardment is done with slow neutrons while  ${}^7_3\text{Li}$  bombardment is done with fast neutrons.  ${}^6_3\text{Li}$  is expected dominate the breeding of tritium in the future reactor despite its low natural abundance, since it is much easier to initiate than the  ${}^7_3\text{Li}$  reaction. The following equations summarize the tritium breeding reactions [5]:



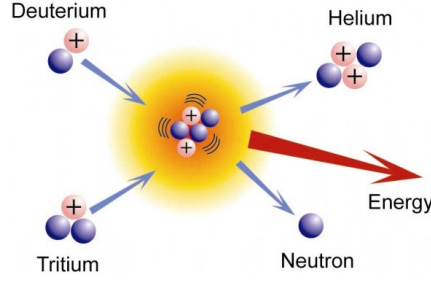


FIGURE 1.2: The D-T nuclear fusion reaction scheme. Very high energy is released as kinetic energy in the process [4].

These reactions are mainly used for tritium breeding in the Lithium blankets used for the plasma vessel, where the energetic neutrons that result from the *D-T* fusion reaction and escape to the blanket vessel first undergo a thermalisation process, and then are used to self-sustain tritium breeding according to reaction scheme in Eq. 1.5.

In order to achieve the required cross sections and reaction rate needed to initiate the *D-T* fusion reaction, the fuel mixture is heated to temperatures of up to 100 million degrees Celsius. Under such extreme conditions of temperature, matter is in plasma state and material walls cannot be used to confine the particles. Plasma consists of charged particles at sufficiently high temperatures to melt the material walls which would contaminate and cool the plasma. To create favourable conditions in the laboratory for nuclear fusion reactions, mechanisms have to be devised to confine plasma. Since the plasma is made of charged particles, the confinement of the particles can be done by using magnetic fields.

## 1.2 Magnetic confinement

In magnetic confinement fusion, a strong magnetic field  $\mathbf{B}$  is used to force particles onto circular or helical orbits perpendicular to the direction of the magnetic field. In this way, the plasma particles are prevented from hitting the walls of the confinement device. The circular motion is due to the magnetic force on charged particles (Lorentz force), which is given by

$$m \frac{d\vec{v}}{dt} = q (\vec{v} \times \vec{B}) \quad (1.7)$$

Here,  $m$ ,  $v$  and  $q$  are the particle's mass, velocity and charge respectively and  $\frac{d\vec{v}}{dt}$  denotes the time derivative of velocity (acceleration of the particle). This force is perpendicular to the direction of the  $\vec{B}$ -field and the particle's velocity. The velocity of the particle can be resolved into perpendicular ( $\vec{v}_\perp$ ) and parallel ( $\vec{v}_\parallel$ ) components. The parallel velocity component is not affected by the  $\vec{B}$ -field, and gives rise to a uniform linear motion along the  $\vec{B}$ -field direction.



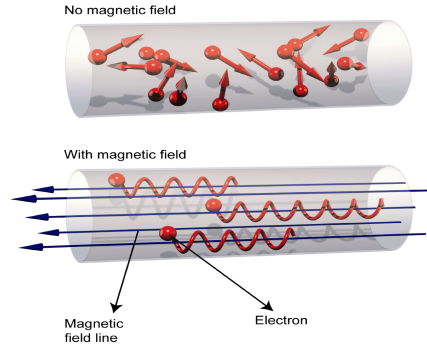


FIGURE 1.3: Effect of magnetic field confinement on electrons. Bottom: With the magnetic field, the particles are confined around the magnetic field lines and forced by the Lorentz force to follow a helical motion along the direction of the field (shown in blue). In this way, they are prevented from hitting the walls of the confinement vessel. Top: Without magnetic field the particles would move randomly in all directions and hit the walls, which would cause damage to the material walls and cooling of the plasma by material contamination [4].

The  $\vec{v}_\perp$  component causes the particle to follow a circular path of motion perpendicular to the  $\vec{B}$ -field, with a gyro- or Larmor radius  $r_L$  given by

$$r_L = \left| \frac{m\vec{v}_\perp}{q\vec{B}} \right| \quad (1.8)$$

The particle's motion is therefore a contribution from the  $\vec{v}_\perp$  and  $\vec{v}_\parallel$  velocity components, which result in a helical motion of the particle along the  $\vec{B}$ -field. The particles gyrate around the  $\vec{B}$ -field lines with a gyro- or Larmor frequency, also called cyclotron frequency  $\omega_L$  given by

$$\omega_L = -\frac{q\vec{B}}{m}. \quad (1.9)$$

Being that the electrons and ions are of opposite charge, they move in opposite directions and, since their masses are different, the electron Larmor radius is much smaller than that of ions.

Applying an external magnetic field by winding current-carrying conductors around the confinement vessel is the best way to concentrate the magnetic field inside a hollow vessel and in this way plasma would be confined in cylinder-like vessel. To prevent it from hitting the cylinder ends, it would require that the cylinder's length is infinite. One way to overcome this would be to use the magnetic mirror effect where  $\vec{B}$ -field inhomogeneities are used to confine the plasma, but the method has proved to be unsuccessful. The only way is therefore to choose the geometry of a torus, where the  $\vec{B}$ -field lines are continuous. The concepts of tokamak and stellarator configurations for plasma confinement are then used.

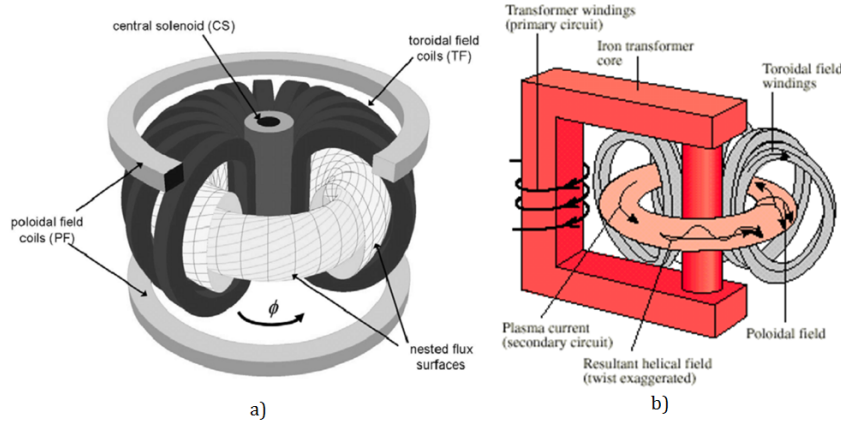


FIGURE 1.4: Magnetic field configuration of a tokamak. The TF coils produce magnetic fields in the toroidal direction, while the poloidal fields (perpendicular to B) are produced by the poloidal field coils and the plasma currents. b) Creation of the poloidal fields by induced currents due to the transformer effect, where a change of flux through the torus induces an electric field which drives the plasma current [6, 3, 2].

### 1.2.1 Tokamaks

The tokamak configuration defines confinement systems with closed magnetic surfaces forming topological tori. The entire toroid cross section is identical, hence making a tokamak to be axis-symmetric. This confinement configuration has by far proved to be the most successful magnetic confinement configuration for plasmas [6, 3, 2].

The resultant  $\vec{B}$ -field strength in a tokamak is a superposition of a strong toroidal field  $B_\phi$  due to the toroidal field (TF) coils, and a poloidal field  $B_\theta$  due to a toroidal plasma current  $I_p$ . Creation of the poloidal magnetic fields in a tokamak is based on the transformer effect, where an iron core solenoid induces a change in flux through the torus and an induced electric field drives the plasma current along the torus axis. The resultant fields are helically twisted, forming nested toroidal surfaces. The poloidal field is much smaller than the toroidal field, which is an order of magnitude higher. Tokamaks are intrinsically pulsed devices, since the induced current can only be maintained while the flux is changing in the transformer. Poloidal field (PF) coils carrying toroidal currents are additionally used for plasma shaping, X-point configuration and control of plasma position. Fig. 1.4 shows the magnetic field configuration of a tokamak and the creation of poloidal fields by transformer effect in a tokamak.

Fig. 1.5 shows two tokamak reactors, JET in the UK is the largest tokamak currently in operation, and ITER is the foreseen experimental reactor which is under construction in France. ITER, though not yet in operation, will be the largest device of its kind in the world.

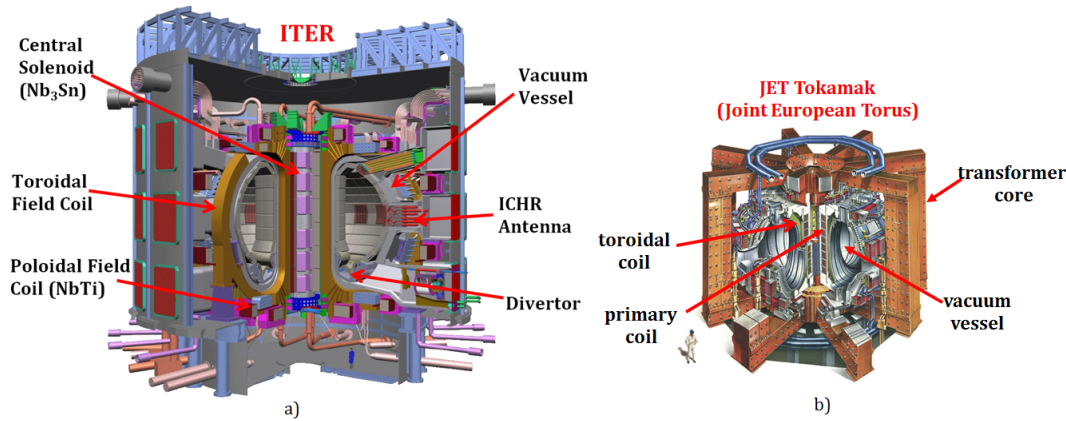


FIGURE 1.5: Reactors based on the tokamak concept. a) The International Thermonuclear Experimental Reactor (ITER), in France. b) Joint European Torus (JET), in the UK [3, 4].

### 1.2.2 Stellarators

Stellarators share the same basic technology with tokamaks but, unlike tokamaks, they are toroidal devices that confine plasma in a magnetic field which originates from currents in coils outside the plasma. No plasma current drive by external means is required for confinement in stellarators. This makes steady state operation in stellarators possible since the lack of a net current avoids current driven instabilities. As a result, there are no disruptions, no resistive wall modes and no conventional or neoclassical tearing modes appearing in stellarators. Steady state operation is therefore an outstanding conceptual advantage of stellarators in addition to the reduction in the recirculation power required in stellarators as compared to tokamaks. With a given magnetic design of the stellarator, second order pressure-driven currents (Pfirsch-Schlüter and bootstrap) that may exist can be modified and even minimized. The magnetic configuration of helical devices naturally possesses a separatrix, which allows the implementation of a helically structured divertor for exhaust and impurity control [6].

The desired poloidal field component supplied by external coils leads to a helically structured plasma topology. Stellarators are therefore fully three-dimensional in contrast to the toroidal (rotational) symmetry of tokamaks [6]. Stellarators are sometimes referred to as helical confinement devices, though the term, in a more strict sense conceptually refers to helical systems where the external currents flow in opposite directions in adjacent helical coils and thus balance, in contrast to heliotrons/torsatrons and heliacs, where a net toroidal current exists in the coil system.

Stellarator equilibrium is not established via the evolving plasma itself, but is to a first order already given by the vacuum magnetic field. Thus, stellarators do not need an active control (like positional feedback) and therefore cannot suffer from its failure. The lack of toroidal symmetry in a stellarator however

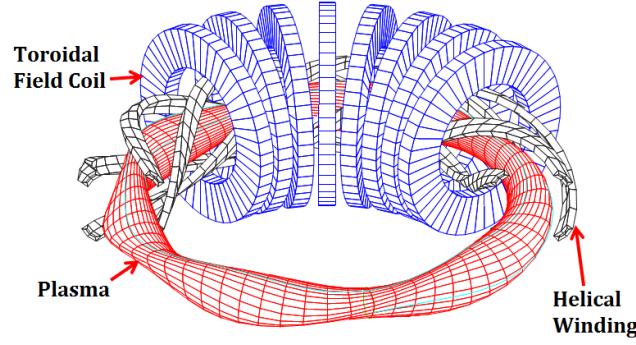


FIGURE 1.6: Schematic of an  $l = 2$  classical stellarator with a circular magnetic axis. Magnetic surfaces are shown in red. The toroidal magnetic field component is created by the planar coils, and the poloidal field by  $l$  dipole coils which wind round the torus circumference [6].

leads to particle drift orbits strongly deviating from the magnetic flux surfaces with the corollary of large neo-classical fluxes, loss of confinement of trapped energetic particles, and to large aspect ratios (which lowers the equilibrium  $\beta$  for low rotational transforms) due to the helical windings used in classical helical devices.

Different stellarator configurations are used, which include the classical stellarator, the heliotron/torsatron, the heliac and the optimized stellarators based on quasi-symmetry and drift optimization [6].

They differ by the magnetic parameters chosen, like rotational transform, magnetic shear, well depth, aspect ratio and the symmetry properties of the magnetic field strength on the magnetic surfaces. The major drawback with the stellarator configuration is that of three-dimensionality, which makes its geometry an engineering constraint. To try to overcome this drawback, attempts have been made to come up with (nearly) two-dimensional systems in an otherwise three-dimensional toroidal geometry. These are referred to as quasi-symmetric systems. Already several stellarators, in particular the quasi-helically symmetric stellarator HSX in Wisconsin, the quasi-axisymmetric device NCSX in Princeton, and the quasi-poloidally symmetric design QPS in Oak Ridge are operated or designed according to these concepts. Fig. 1.6 shows a schematic of an  $l = 2$  classical stellarator.  $l$  planar or helical coils which wind toroidally round the torus  $n$  times provide the poloidal magnetic field component.

The largest advanced stellarator which is currently under construction is the Wendelstein 7-X, in Greifswald, Germany. It follows the quasi-isodynamic/quasi-omnigenous design principle in which the desired optimization criteria is achieved by a minimization of the geodesic curvature of the flux surfaces. The largest currently operational stellarator in Europe is the TJ-II stellarator in CIEMAT, Madrid-Spain. The heliac stellarator concept (HELical Axis Configuration), as in the TJ-II, makes use of coils placed helically around a circular central

coil, to produce the poloidal field and allows additional flexibility in the setting of the rotational transform. The result is a plasma column with a bean-shaped cross-section and a helical magnetic axis that spirals around the circular conductor.

In a heliac machine, a magnetic well is realized, which ensures good MHD stability properties. The heliac offers a high degree of flexibility so that important equilibrium, stability and transport issues can be addressed [6].

## 1.3 Plasma heating

The steady state power balance condition in a D-T fusion reactor demands that the following conditions of pressure ( $p$ ), temperature ( $T$ ), plasma density ( $n$ ) and energy confinement ( $\tau_E$ ) are fulfilled for ignition, so that the alpha particle heating is sufficiently large to balance the combined bremsstrahlung and thermal conduction losses without need for external power.

$$nT\tau_E > 3 \times 10^{21} \text{ m}^{-3} \text{ keVs}. \quad (1.10)$$

In order to reach the minimum  $n\tau_E$ , external power has to be supplied for heating the plasma. Even for an optimized reactor situation in which steady state power balance is reached without external heating, external power will still be needed during the start-up transient phase to heat the plasma from the initial low temperature to a high enough value for the alpha heating to become dominant. External heating of plasma is therefore a necessary evil for a fusion reactor operation.

The main external plasma heating schemes used in nuclear fusion reactors are discussed in the paragraphs that follow.

### 1.3.1 Radio frequency (RF) heating

In RF heating, high frequency electromagnetic waves are launched into the plasma from an external source at the outer edge of the plasma, and the waves propagate up to the desired location in the plasma where absorption of power in the form of heat takes place. Plasma heating is done at selected resonant frequencies of the plasma. When the waves interact with the plasma particles, resonant wave absorption takes place by collision-less damping. Three different methods are used, which are described according to the range of frequencies at which the waves can be launched:

1. Electron Cyclotron Resonance Heating (ECRH)

This involves heating of the plasma at the cyclotron frequency of the electrons. The ECH waves are launched at frequencies in the range of  $\sim 10\text{--}300$  GHz. RF mirroring systems are used to launch the ECH waves to the plasma. The transmission of the ECH power is done using waveguides of relatively small cross sections. ECH use is however still

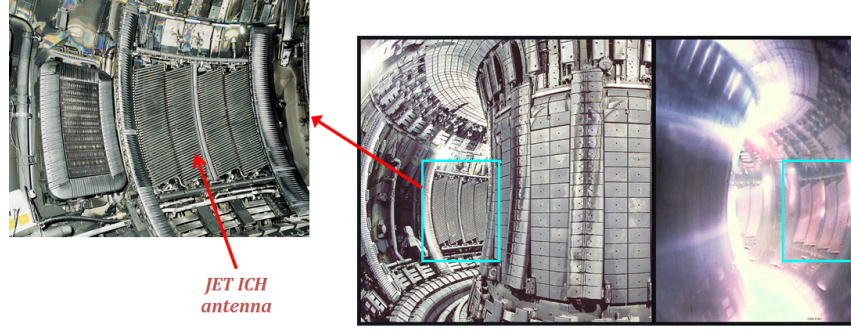


FIGURE 1.7: The JET ICRH launching antennas in the vacuum vessel [3].

faced with technological challenges, as steady state gyrotron sources at the required frequencies are still not yet readily available.

## 2. Ion Cyclotron Resonance Heating (ICRH)

Here, heating is done at the ion cyclotron frequencies ( $\sim 40\text{--}100\text{ MHz}$ ). High power vacuum tubes are used as a source of the ICRH waves, and their transmission is done by use of parallel wires or coaxial transmission lines. The ICRH launching structures are antennas placed inside the vacuum vessel. The requirement that the launching antennas are placed very close to the plasma surface for good wave-plasma coupling in ICR heating leads to problems of impurities in plasma, arcing and plasma breakdown. The method is therefore faced with technological challenges in designing launching antennas well-shielded enough to prevent high-voltage arcing. Fig. 1.7 shows an ICRH launching antenna in JET.

### 1.3.2 Neutral beam injection (NBI) heating

In NBI heating, high energy beams of neutral deuterium are injected into the plasma. The beam atoms propagate in a straight line and are able to propagate into the vacuum vessel of the plasma machine since they are not affected by the strong magnetic fields of the coils. Once the neutral atoms get into the plasma, they are ionized by collisions with the plasma particles (ions and electrons). The ionized particles then give up their energy to the plasma by collisions when the beam energies are much higher than the plasma temperature. For good NBI heating, it is important that the neutral beam is capable of penetrating to the centre of the plasma. In the rest of this document NBI heating system of the TJ-II is dealt with, and therefore more about plasma heating by the NBI will be discussed in the due course.

# Chapter 2

## NBI heating systems

To produce a high power neutral beam, an ion beam must be generated, neutralized, and transported to the plasma vessel. All existing NBI systems, within a wide range of beam energy and power, contain the same components, with variations in the applied technologies but not in the concept or outline of the beamlines.

### 2.1 Neutral beam generation and transport

The NBI beamline system is made up of the Ion Source (where the ions are extracted and accelerated), the Neutralizer (a gas-filled charge exchange cell), the Ion Removal system, made up of a bending (or deflection) magnet (BM) with the ion dump, a movable calorimeter (target), and a drift tube/beam duct to mechanically couple the Beamline and the magnetic confinement machine. Fig. 2.1 presents a schematic view of a beamline with its main components.

#### 2.1.1 Ion source

Ion sources consist generally of a plasma source and an ion extraction and acceleration system. In an Arc plasma source as the one depicted in Fig. 2.2, the

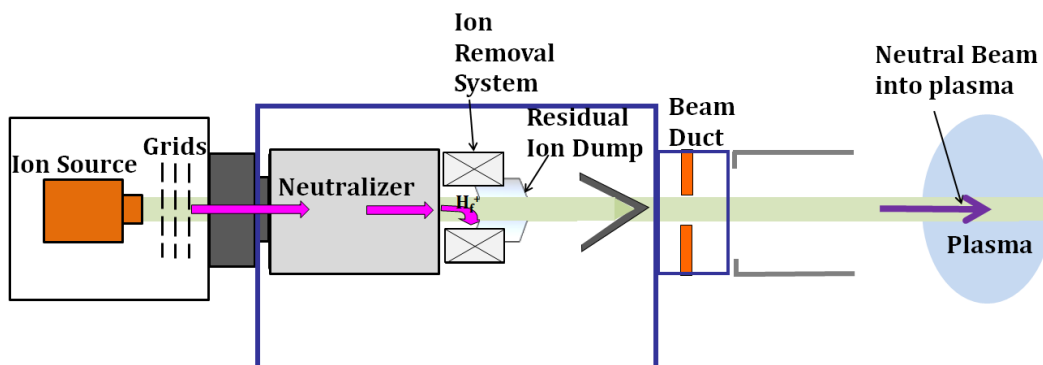


FIGURE 2.1: NBI system components.



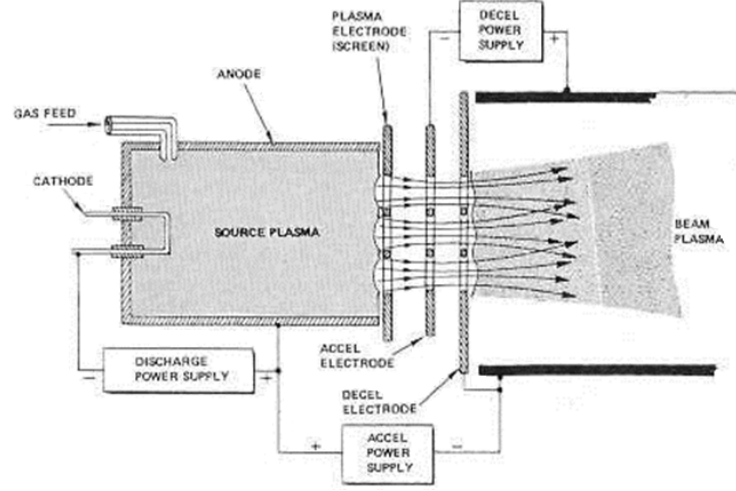


FIGURE 2.2: Schematic of an ion beam generating system[7].

plasma is generated by applying a voltage of around 100 V between an electron-emitting cathode and an anode, in a chamber where the required gas is present. The emitted primary electrons generate the plasma by collisions with the gas molecules. Plasma densities range between  $10^{10}$  and  $10^{16} \text{ cm}^{-3}$  and electron temperatures lie typically between 5 and 10 eV. In a Hydrogen discharge, three main ion species are generated:  $H^+$ , and the molecular ions  $H_2^+$  and  $H_3^+$ , their relative ratios being determined by plasma and wall conditions.

Positive hydrogen ions are electrostatically extracted from the plasma source and accelerated to energies of several tens of kilovolts by the high voltage (V<sub>acc</sub>) between the perforated extraction and acceleration electrodes (the grids). The extracted ion current ( $I_{\text{acc}}$ ) is basically determined by the plasma density, which is controlled by the Arc voltage and neutral gas density. The electrical power generated by the Accel Power Supplies is typically several MW for the existing systems, although considerably larger powers will be needed at ITER and DEMO (40 MW).

The positive ions are not emitted from a solid surface but from a curved surface (plasma “meniscus”) whose radius of curvature is determined by the self-consistent space-charge-limited flow of ions [8]. A negatively biased electrode, also called the suppressor electrode or decel electrode, is also used, which prevents the backward acceleration of the neutralizer plasma electrons to the plasma source by creating a potential well, and also gives rise to the electrostatic divergent lens effect upon the ion beam. Backward acceleration of the electrons would constitute an electron current which would pass through the accelerating power supply and cause current (and power) drain from the supply.

The beam quality is determined by the trajectories of the ions, which in turn, are dependent upon the strength of the applied field, the shape of the emitting surface, and on the resulting space-charge density due to the beam. It is



therefore essential that the best beam quality is achieved right from the level of the extraction system since less control is possible of the neutral beam along its trajectory after extraction [8].

The geometrical design of the extraction system therefore determines the overall performance of the injection system, and considerable effort is always devoted to its optimization.

### 2.1.2 Neutralizer

The neutralizer is a drift tube coupled to the ion source and is supplied with a cold gas flow in addition to the flow out of the ion source to create a gas target density inside it for the conversion of the ions into neutrals. The fast ions are neutralized via charge exchange collisions with hydrogen molecules present in the neutralizer.

In the neutralizer, the two molecular ion species  $H_2^+$  and  $H_3^+$  undergo dissociative collisions with the gas molecules  $H_2$ , resulting in the final mix of three monoatomic neutral species of full energy  $E$  (from  $H^+$  ions), half energy  $E/2$  (from  $H_2^+$  ions), and third energy  $E/3$  (from  $H_3^+$  ions) with varying ratios.

### 2.1.3 Ion removal system (bending magnet (BM) and ion dump)

The beam that leaves the neutralizer towards the plasma machine contains residual (un-neutralized) ions that escaped neutralization. Non-neutralized ions in the beam represent a considerable amount of power, especially for high energies (neutralization efficiency is less than 40 % for energies greater than 60 keV/amu). Under the residual magnetic field of the plasma confinement machine the trajectories of the un-neutralized ions may hit the inner surfaces of the beamline at unwanted locations causing significant damage due to thermal overload, and leading to enhanced gas desorption and collisional beam losses.

To avoid such undesirable effects, an ion removal system is necessary for controlled removal and thermalisation of their power on a suitably designed ion-dump before the beam enters the field of the plasma machine. In most NBI systems the ion removal system consists of a magnetic deflection system – the “Bending Magnet”- and a heavily cooled target – the “Ion Dump”.

### 2.1.4 Beamline Calorimeter

A V-shaped copper calorimeter target is generally used to intercept the full beam inside the beamline vacuum vessel. To handle the large thermal loads generated by the absorbed beam power, an efficient cooling system is required. Water circuits thermally coupled to the target material perform the heat removal either “inertially” (between beam pulses) or “actively” (during the beam pulse). The beam transmission can be measured by water calorimetry at the

V-calorimeter, as the ratio between the full beam power at the calorimeter and the extracted beam power at the ion source.

### 2.1.5 Beam duct

The beam duct is the vacuum vessel connecting the beamline and the plasma machine. It is generally a long (1–10 m) and narrow (0.5–1.0 m diameter) drift tube without local vacuum pumps, therefore the most critical component for beam transmission.

### 2.1.6 Primary vacuum system

Fast vacuum pumping is required to remove the gas present in the beamline during the beam pulses, in order to maintain the collisional losses at a minimum level. The elevated pumping velocities in the range of  $500,000 \text{ l.s}^{-1}$  are obtained with cryogenic or titanium getter pumps.

## 2.2 Beam transmission

Of the total beam power generated at the Ion Source, only a fraction (25–35 %) reaches the plasma. The beam power loss can be assigned to two different mechanisms: collisional losses due to the fast particle interactions with the residual gas along the beam path, and geometrical losses due to interception of the unavoidably divergent beam with the beamline and duct apertures.

A sufficiently thick gas target is required at the neutralizer for optimum neutralization, but the gas drifting out of the neutralizer together with gas re-emitted by surfaces under beam direct impacts give rise to reionization reactions in the beamline and beam duct that translate into power losses.

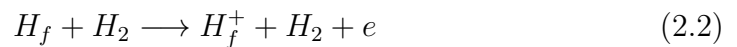
The overall beam transmission is determined by the following three mechanisms: Neutralization losses, reionization losses and geometrical losses.

### 2.2.1 Neutralization losses

Neutralization of the ions takes place by charge exchange reactions of the fast  $H^+$  ions ( $H^+$ ,  $H_2^+$ ,  $H_3^+$ ) with the slow  $H_2$  molecules in the neutralizer. The neutralization reaction has a cross section,  $\sigma_{10}$ , which depends on the ion energy-to-mass ratio.



However, ionization of the fast neutrals also occurs in the neutralizer through collisions of the fast neutrals with the gas molecules, with cross section  $\sigma_{01}$ .



Inside the neutralizer as the fast ion population decreases, so does the neutralization reaction rate, whereas the growth in fast neutral population

leads to an increase of the ionization reaction rate. The two beam fractions (neutrals and ions) then asymptotically approach equilibrium for an increasing neutralizer target thickness as the neutralization and ionization rates balance out. From the balance equation for the two reactions in Eq. 2.1 and 2.2 above, a relation is found [8] for the asymptotic neutralization fraction  $F_0^\infty$  (a measure of the ratio of neutral current to the total current for an infinitely thick neutralizer) [8]:

$$F_0^\infty = \frac{\sigma_{10}}{\sigma_{01} + \sigma_{10}} \quad (2.3)$$

The two cross sections  $\sigma_{10}$  and  $\sigma_{01}$  are only dependent upon the energy per nucleon of the fast particles, and so is  $F_0^\infty$  which has been found to decrease (while the required target thickness increases) with increasing particle energy. Positive ion beams with energy over a hundred keV/amu will have very low neutralization efficiency ( $< 10\%$ ) [8]. In ion sources based on positive ion extraction, as is the case for most existing systems, the above expression for the asymptotic neutralization fraction  $F_0^\infty$  must be averaged over the three beam energy species ( $E$ ,  $E/2$ , and  $E/3$ ) weighted with the corresponding abundance rates. The averaged energy beam energy is lower than the full beam energy.

### 2.2.2 Re-ionization losses

The re-ionization reactions of the fast neutrals leaving the neutralizer with the gas molecules present in the beam path result in a loss of beam power [8].

The reionized fraction of the beam can be expressed as:

$$F_R = n_{H_2} \cdot \sigma_{01} \cdot L, \quad (2.4)$$

where  $n_{H_2}$  is the particle density of the neutral gas,  $\sigma_{01}$  is the reionization cross section, and  $L$  is the reionization path length. The reionization cross section for fast  $H^0$  neutrals in a  $H_2$  gas target increases with the  $H^0$  energy up to 45 keV, where it hits a maximum after which the cross section decreases with increasing energy [9].

The resulting charged particles from re-ionization are deflected by the residual magnetic ( $\vec{B}$ ) field of the machine and their trajectories do not reach the plasma. Besides, when the deflected ions hit the vacuum vessel walls, re-emission of adsorbed gas results from these surfaces. Re-emitted gas adds to the gas target for reionization which behaves as a cascade process.

Under very unfavorable conditions (poorly conditioned duct) re-ionization losses can lead to total beam blocking and a large gas and impurity load into the plasma machine, sometimes resulting in a thermal and radiative collapse of the plasma [10]. Re-ionization losses may represent a significant fraction of the total beam power, and the gas re-emission must be minimized.

### 2.2.3 Geometrical losses

#### 1. Single aperture extraction system

In a single aperture extraction system such as the one depicted in Fig. 2.3,

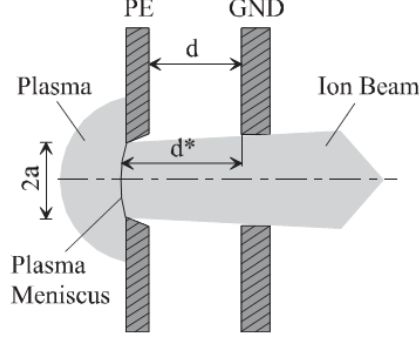


FIGURE 2.3: Two electrode single aperture extraction system. The plasma electrode (PE) and ground electrode (GE) are shown, separated by a distance  $d$  [12].

the ion emitting surface is the curved interface between the plasma region (where the electric field is close to zero due to plasma quasi-neutrality) and the high electric field region between electrodes. The shape of this interface (the “meniscus”) depends on the plasma density and temperature, and the electrostatic potential. Ion trajectories are determined by the shape of the meniscus, the space charge associated with the ion flux, and the electric potential distribution between the electrodes.

Experimental and analytical studies of the beam optics of a single aperture extraction electrode system (a single beamlet) have shown that, for a given extraction geometry, there is an optimum relationship between the flux density of the ions and the electrostatic potential difference  $V$ , such that the resulting plasma curvature yields a minimum beam divergence [11, 8].

Ion extraction from a single aperture is a space charge limited process that can be described along the lines of the Child-Langmuir law. When applied to positive ions extracted from a spherical plasma emitter it yields [11, 12, 8]:

$$I = C \times V \times \left( \frac{Z}{M} \right)^{1/2} \times \left( \frac{a}{d} \right)^2, \quad (2.5)$$

where  $I$  is the extracted current,  $C$  a constant,  $V$  is the applied electrostatic potential,  $Z$  and  $M$  are the charge and mass number of the extracted ion,  $a$  the aperture radius, and  $d$  the gap between plasma and suppressor electrodes. The aspect ratio  $a/d$  is a measure of the field distortion due to the difference in field strengths on each side of the accelerating grid aperture (distortion increases with the aspect ratio), and it strongly contributes to the beam divergence. It is constant for a given extraction system, and since for a given extraction system  $Z/M$  is also constant, the ion beam current that can be extracted with optimum transmission is therefore proportional to  $V^{3/2}$ .

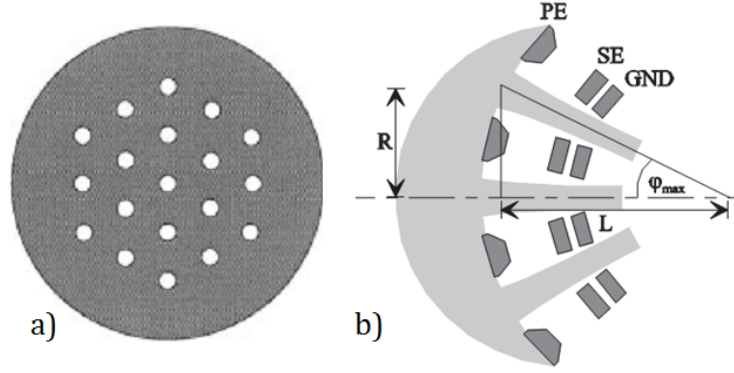


FIGURE 2.4: Multi-aperture extraction. a) Front view of a multi-aperture extraction electrode. b) Spherical extraction of a multi-aperture extraction system. The plasma electrode (PE), secondary electrode (SE) and ground electrode (GND) are shown in b). Individual beamlets contribute to the overall intensity distribution to form a Gaussian distribution profile at the focus [12].

The beam perveance  $p$  is defined by the ratio

$$p = \frac{I}{V^{3/2}}. \quad (2.6)$$

The optimum perveance (the one that yields minimum beam divergence) is therefore determined by the geometrical properties of the extraction grid, specifically by the aspect ratio  $a/d$ , and by the charge-to-mass ratio  $Z/M$  of the extracted ion. From Eq. 2.5, it would require large apertures and close grids to obtain large ion currents. However, because of the danger of a high voltage breakdown on the grid system, there is a minimum  $d$  for a given voltage [11, 12, 8]. For good divergence, the aspect ratio, therefore the extraction aperture, must be small. Therefore, to achieve high current low divergence beams, a multi-aperture extraction system must be used.

## 2. Multi-aperture extraction system

To maximize the beam transmission through the duct, the extraction grid has to be designed such that the individual beamlets are steered to a common focus near the entrance of the plasma device. Each beamlet propagates with an expanding Gaussian profile whose centre is directed towards the focal point  $F_i$ . The total beam power at any position is the sum the power contributions from all the individual beamlets at that point. A multi-aperture extraction electrode is shown in Fig. 2.4.

Each individual beamlet contributes an intensity  $i_b$ , represented by a Gaussian profile, to the total beam power at a given localized position.

$$i_b(d, \rho) = \frac{i_0}{\pi \cdot a^2} \exp\{-\rho^2/a^2\} \quad (2.7)$$

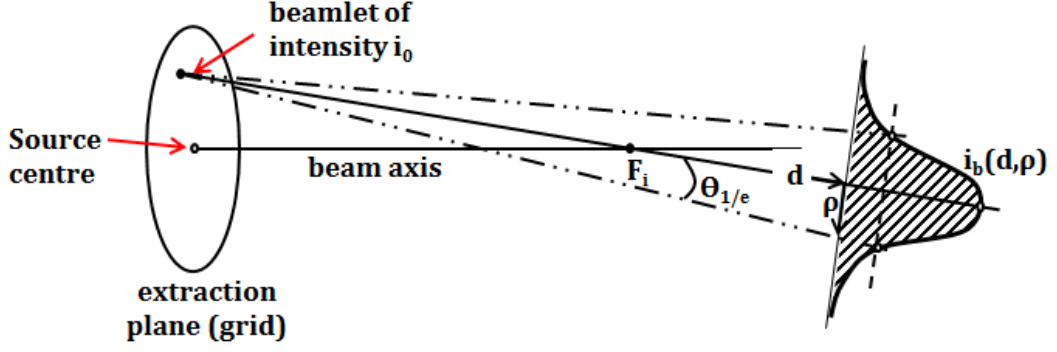


FIGURE 2.5: A contribution of one beamlet in a single multi-aperture source. Individual beamlets propagate with an expanding Gaussian profile whose centre is directed towards the focus  $F_i$ .

Here,  $a = d \cdot \tan \theta_{1/e}$  is the  $1/e$  profile width with  $1/e$  half-divergence angle  $\theta_{1/e}$ ,  $\rho$  is the radial distance from the beamlet profile maximum at distance  $d$ ,  $i_0$  is the total power of the beamlet and  $d$  is the axial distance from the beamlet centre [see Fig. 2.5 below for geometrical details]. The combined beam intensity for a multiaperture system due to the contribution of all individual beamlets at an axial distance  $d$ , can be derived and is shown to be an exact Gaussian at the focal plane ( $d = f$ ) [13]:

$$i_b(f, \rho) = \frac{i_0}{\pi a(f)^2} e^{-\rho^2/a(f)^2}. \quad (2.8)$$

Here  $a(f) = f \cdot \tan \theta_{1/e}$ .

Eq. 2.8 shows the convolution of all beamlets into a Gaussian at the focus.

Variations in power density with the axial distance from the source are a result of two combined effects: the divergence of single beamlets represented by the  $1/e$  width, and the overlapping of beamlets due to the beam focusing.

## 2.3 Motivation

Neutral Beam Injectors are used for plasma heating and as a source of particles for the plasma (plasma fueling). The beam contributes to plasma fueling in two different ways: as fast beam ions trapped by the plasma and confined inside it, and as cold gas re-emitted (through thermal and impact desorption) from surfaces intercepted by the beam particles.

The re-emitted gas has two undesirable effects: it creates a gas target for beam re-ionization (re-ionized neutrals are lost to the plasma), and also it contributes to plasma fueling, though not in the controlled way of the gas puffing system, where the gas flow can be integrated in a feedback loop, but in a rather uncontrolled fashion.

NBI transmission optimization is necessary in order to deliver maximum power and fast particle current to the plasma, and to minimize beam interception by surfaces thereby reducing gas re-emission.

Improving the NBI efficiency is relevant in all present day machines, but is of critical importance in ITER and DEMO, where the huge power demands may jeopardize the achievement of the  $Q$  factor objectives.

In TJ-II, as in all stellarators, the pronounced helicity of the heliac configuration complicates beam access to the plasma, since the injection port and duct must be accommodated between the narrow space available between two neighbouring toroidal field coils. Therefore, beam transmission optimization needs to be carried out with particular care.

To study the behaviour of NBI heated plasmas, it is necessary to have a correct knowledge of the beam power balance. In TJ-II, attainment of the high confinement mode (“H-mode”) is the object of sustained effort in the latest campaigns, with particular attention being given to the beam power threshold [14]. The beam power coupled to the plasma is usually estimated through beam simulation codes that need to make a number of assumptions related to beam transmission in order to estimate the power that reaches the plasma. It is highly desirable to develop the use of adequate experimental tools to obtain a good estimate of that power, within the unavoidable uncertainties.

On the other hand, a series of experiments have been carried out at TJ-II during the last experimental campaign, aiming to study the effect of the fast ions on the excitation of MHD modes in the plasma [15]. The so-called Alfvén eigenmodes have been shown to produce a deleterious effect on the fast ion confinement, with associated losses as great as 40 % in some published studies [16]. In the TJ-II experiments the beam energy and beam current of the injected beams have been varied in order to separate the influence of those parameters on the Alfvén wave excitation mechanism [17]. For the correct interpretation of the results, it is of primary importance to determine the beam particle transmission to the plasma corresponding to each set of beam parameters.

Beam transmission, in a broad sense, includes: beam neutralization, geometrical transmission (beam optics and divergence) and re-ionization (collisional losses).

In this work, use of conventional tools such as water calorimetry is made of for the determination of the neutralization fraction and the geometrical transmission at the V-Calorimeter located inside the beamline chamber. Infrared thermography is used to study the beam profile at the Target Calorimeter, placed at the TJ-II entrance, where the beam focus is located. From the beam power density profile the  $1/e$  beam divergence can be obtained. Finally, infrared thermography of the Beam Stop plate, at the beam exit, allows the estimate of the re-ionization losses associated to the gas target created by re-emitted gas. Use is also made of Fast Ion Gauges (FIG’s) to measure the pressure rise at the duct during beam pulses and study the correlation between residual gas pressure and reionization losses.

To obtain the beam power and beam particle current that reach the plasma, the results of these measurements must be combined with a beam simulation code -DENSEB- that studies the transmission of a beam of given divergence. Those beam simulation studies lie outside the scope of this work, being left as the subject of future analysis based on the outcome of the present experiments. The beam geometrical transmission is a key factor in efficiency optimization and will be the main focus of this work. The geometrical transmission has a strong dependence on beam parameters such as the beam current and acceleration voltage through the beam perveance ( $p = I/V^{3/2}$ ).

In this study, perveance scans are carried out in two different ways: energy scans (varying beam acceleration voltage,  $V_{\text{accel}}$ , at constant current) and current scans (varying beam current,  $I_{\text{accel}}$ , at constant acceleration voltage). Beam transmission is studied as a function of perveance at three different locations along the beam path; the V-calorimeter - to study transmission from the ion source to the duct entrance, the Target Calorimeter (TC) at the beam focal position - to study transmission through the beam duct and to estimate the power distribution across the beam cross section, and the Beam Stop (BS) positioned inside the TJ-II vacuum chamber - to study transmission to the beam “exit/back plate”.



# Chapter 3

## Neutral Beam Injection at TJ-II

### 3.1 The TJ-II stellarator

The TJ-II is a flexible, medium-size stellarator of heliac type belonging to the National Fusion Laboratory of Spain, a department within the “Centro para Investigaciones Energéticas, Medioambientales y Tecnológicas”, CIEMAT (literally referred to as the Centre for Energy, Environment and Technology Research), Madrid (Spain). CIEMAT is an organ of the Spanish Ministry of Science and Innovation.

TJ-II was designed in an effort to study the physics of magnetically confined plasmas, with emphasis on the influence of the magnetic configuration on heat and particle transport, which would contribute significantly to the international efforts towards developing magnetic confinement fusion as an energy source, and is currently the largest operational stellarator in Europe [18]. It was designed in collaboration with the Oak Ridge National Laboratory (ORNL) group, USA. TJ-II experiment was designed as a device with enough flexibility to cover a wide range of rotational transform values.

The TJ-II configuration is shown in Fig. 3.1: it basically consists of 32 toroidal field (TF) coils whose centres follow a toroidal helix of major radius  $R_0 = 1.5$  m and two poloidal coils, called the Central Conductors (CC), consisting of a circular coil centered at the major axis (1.5 m) and a helical winding wrapped around the circular coil following the same winding law as the TF coils.

TJ-II’s unique flexibility is achieved by the separately controllable currents in the hard core windings. The coil configuration is completed by two circular vertical field (VF) coils which add a vertical magnetic field of about 5 % of the TF strength and are used to control the position of the magnetic axis. As shown in Fig. 3.1b., the TJ-II magnetic surfaces are bean-shaped for the entire operational space. The high degree of flexibility in TJ-II makes it a very attractive device to study the stability properties of helical-axis plasmas with a broad range of rotational transform and magnetic well values.

In TJ-II, ECRH and NBI systems are used to heat the plasma. ECR heating is done in the second harmonic, using two gyrotrons, each of 350 kW and working at 53.2 GHz [19]. In order to reach the central  $\beta$  values of 3–4 %

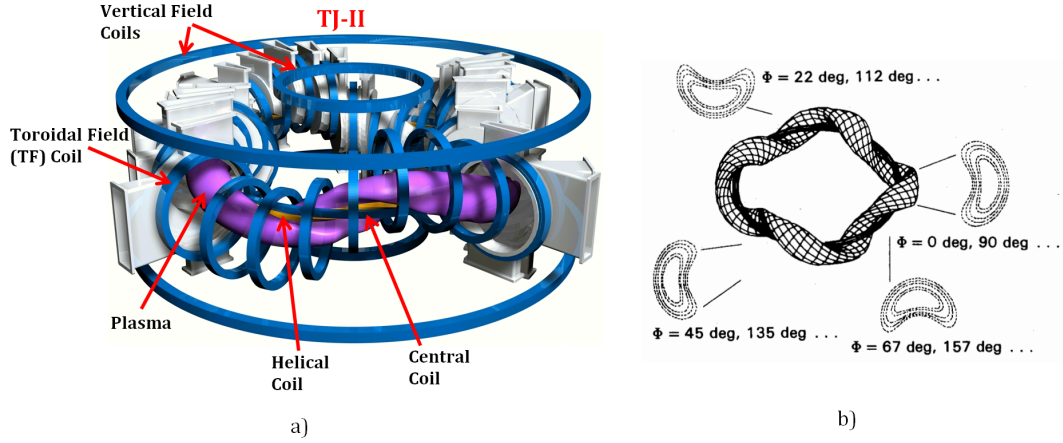


FIGURE 3.1: TJ-II stellarator. a) The plasma winds helically around two central conductors: a circular and a helical conductor surrounded by a steel hard core. b) TJ-II coil configuration [18, 19].

needed to demonstrate the good stability properties of the heliac plasmas, two balanced (Co-Counter) neutral beam injectors are used [20]. The main parameters of the TJ-II are summarized in Tab. 3.1.

## 3.2 The NBI system at TJ-II

Two NBI lines [21] in a tangential Co-Counter configuration inject two  $H^0$  beams of energies between 30 and 40 keV and total injected power between 1 and 1.5 MW. Fig. 3.2 shows a photograph of TJ-II with the two NBI beamlines.

The plasma sources are of the DuoPIGatron kind [22, 23] developed at ORNL (USA) along the 1970s and 1980s. It is an arc discharge source that provides up to 1200 A of plasma current between the anode and the cathode. Electron emission takes place at the hot cathode, and the emitted electrons are accelerated by a DC voltage of 150 V into the anode chamber, where the desired arc plasma is produced by ionization of the gas molecules. In order to optimize the ionization efficiency of the fast electrons, a confining magnetic field is provided by a solenoid coaxial with the source. DuoPIGatron sources have been shown to have a high gas ( $\sim 35\%$ ) and high arc (0.56 A/kW) efficiencies [23].

At the 3-grid system (of 30 cm diameter) an ion beam of up to 100 A current (Iaccel) is extracted and accelerated by applying a high voltage between 30 and 40 kV. The Ion Source parameters are summarized in Tab. 3.2.

The 3-grid system produces a beam of nominal  $1/e$  divergence 1.30. Geometrical transmission into TJ-II has been studied by means of the 3D geometric code DENS B [24]. The drift duct which is currently in place is designed such that the overall geometric transmission including the first toroidal field coil is around 62%.

Parameter	Value/Range
Major radius, $R_0$ (m)	1.5
Average magnetic field, $\vec{B}_0$ (T)	1
Minor radius, $a$ (m)	0.1–0.25
Number of periods	4
TF coil radius (m)	0.425
Number of TF coils	32
VF coil radius (m)	2.25
rotational transform at $\vec{B}$ –axis	0.96–2.5
Working gas	Hydrogen
Plasma volume (m <sup>3</sup> )	1
Electron density, $n_e$ (m <sup>-3</sup> )	$8 \times 10^{19}$ (NBI), $1.5 \times 10^{19}$ (ECRH)
Ion temperature, $T_i$ (eV)	150
Electron temperature, $T_e$ (keV)	2

TABLE 3.1: Design parameters of TJ-II stellarator and its plasma parameters [18, 19].

Parameter	Value/Range
Working gas	Hydrogen
Accel voltage (kV)	40
Accel current (A)	100
Decel voltage (kV)	1.5
Decel current (A)	10
Arc voltage (V)	150
Arc current (A)	1200
Pulse length (ms)	300
Duty cycle (%)	$\leq 1$
Gas throughput (Torr.l.s <sup>-1</sup> )	20–40

TABLE 3.2: Operating parameters of the TJ-II NBI system [20].

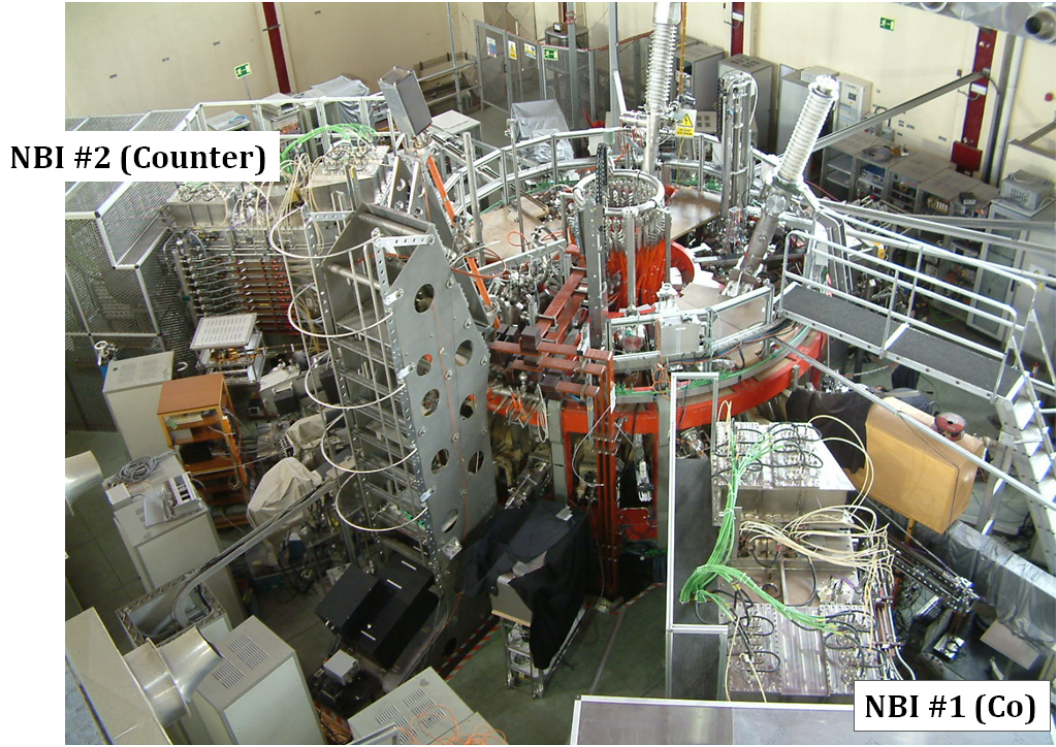


FIGURE 3.2: The NBI beamlines at TJ-II.

Due to losses of geometrical and collisional origin, the estimated power “Through Port” is only about 35 % of the total ion beam power. This figure includes the neutralization losses, geometrical and re-ionization losses inside the beamline. The reionization losses depend on the residual gas pressure inside the beamline. Calculations performed with the NBI simulation code OPTIMUS have shown [21] that in order to keep re-ionization losses below 10 % during the beam pulse, the maximum pressure must be below  $10^{-4}$  mbar. To maintain this low pressure, the necessary pumping speed in the beamline vacuum vessel is  $350,000 \text{ ls}^{-1}$ . Four Titanium getter pumps constitute the primary vacuum system of the beamlines, that provide the required pumping speed.

The beam duct is a 1 m long vessel with internal diameter 300 mm [20], which connects the beamline vessel with the off-axis rectangular injection port. A side view of one injector with the duct connection to TJ-II is shown in Fig. 3.3. The dimensions of the beam duct and consequently the beam transmission are severely restricted by the helical geometry of TJ-II. Direct beam interception by material surfaces in the injection path gives rise to high power loads at localized areas. The beam duct has been designed to withstand high power densities of up to  $8 \text{ MWm}^{-2}$  for beam pulses of 300 ms. Graphite plates are used to protect the vessel walls at the critical areas in the beam ducts and TJ-II vacuum vessel.

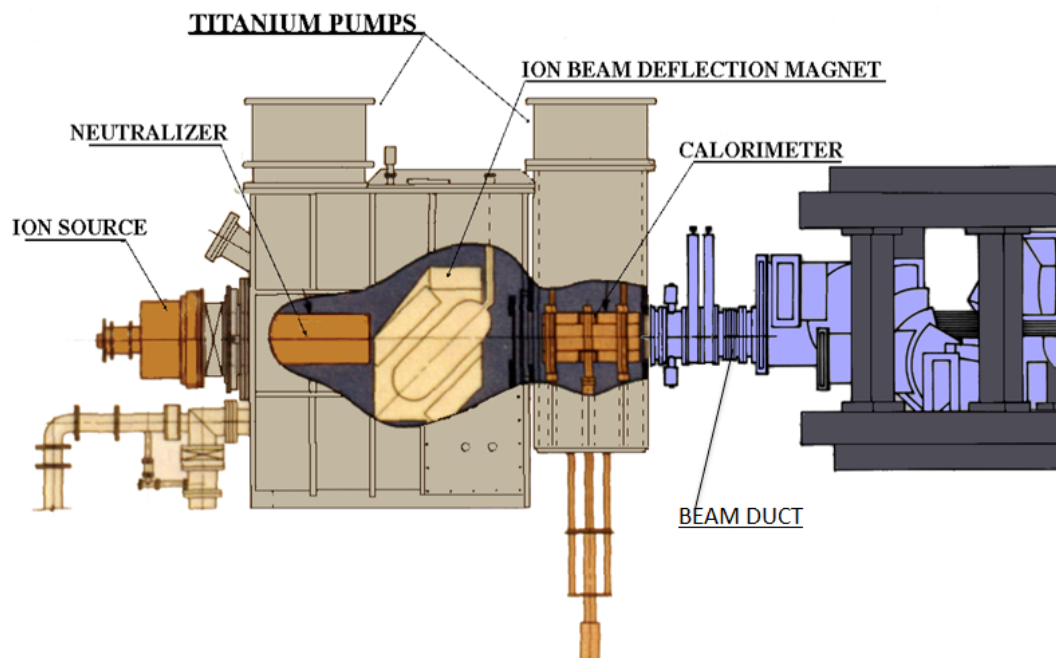


FIGURE 3.3: Side view of one injector with the duct connection to TJ-II.



# Chapter 4

## Methodology and Diagnostic techniques

To monitor the beam transmission in TJ-II, the power deposition on three targets located at different distances along the beam path was studied. In Fig. 4.1, the positions of the three targets are schematically presented. The V-calorimeter was used to monitor the transmission from the ion source through to the beam box exit, the Target Calorimeter (TC) at the beam focus to study transmission through the beam duct, whereas the Beam Stop (BS) inside the TJ-II vacuum chamber was used to monitor the transmission up to the beam “exit”. These measurements, performed for a series of beam pulses with parameter variation scanning a wide range of perveance values, allow for a comparison of the beam power at the three targets and enable us to obtain the beam power transmission as a function of perveance, an estimate of the beam re-ionization losses, and the beam profiles as a function of perveance, from which the net beam power delivered to the plasma can be obtained. The major diagnostic techniques that were used are: water calorimetry of a copper target at the V-calorimeter and Infrared thermography on the TC and BS. Fast ion gauge (FIG) measurements were also used to monitor the pressure build up in the beam duct.

In order to be able to use the temperature measurements from the TC and BS targets as a straightforward measure of the incident power density, the target must satisfy the semi-infinite solid approximation. Here, a brief discussion to introduce the semi-infinite solid approximation is given.

### 4.1 The semi-infinite solid approximation

In the interpretation of the diagnostic signals used on the three targets (V-Calorimeter, TC and BS), the semi-infinite solid approximation is used. The approximation is valid for all the targets, as shown in the material properties summarized in the Tab. 4.1 and 4.2.

When the neutral beam hits the material target, it deposits its energy on

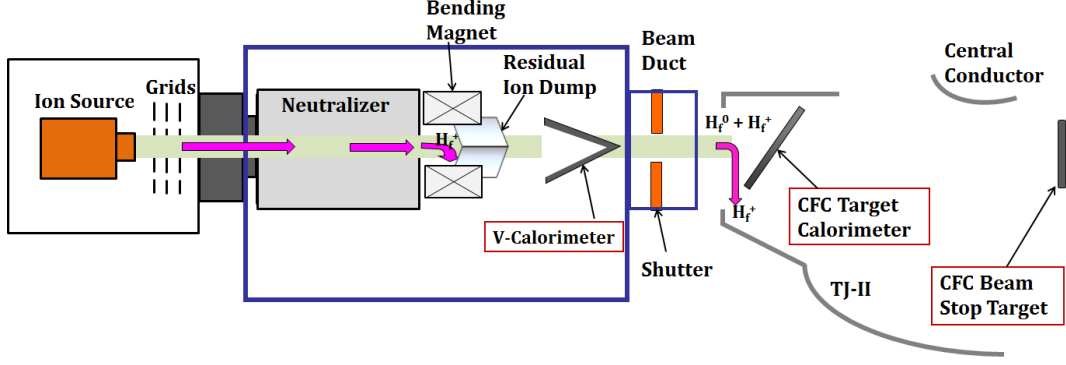


FIGURE 4.1: Schematic drawing showing the TJ-II NBI components and the diagnostic target positions. The V-Calorimeter, Target Calorimeter and Beam Stop targets are shown.

the surface from where the heat propagates into the material bulk, setting up a non-steady state conduction process governed by the material thermal constants. For the thermographic measurements, the surface temperatures are monitored with an infrared camera during and after the pulse. Similarly, the energy carried by the beam is deposited on the copper surface of the V-Calorimeter, and the heat generated propagates through the plate thickness by conduction [25].

A simplified approach to the problem is to consider the target as ideally represented by a semi-infinite solid, whose surface is hit by a constant and uniform power flow  $P_0$ . The differential equation describing the temperature evolution in the solid bulk is:

$$\kappa \frac{\partial^2 T}{\partial x^2} = \frac{\partial T}{\partial t}, \quad x > 0, t > 0 \quad (4.1)$$

where  $\kappa$  is the thermal diffusivity through the solid given by

$$\kappa = \frac{K}{\rho \cdot c_p}, \quad (4.2)$$

$K$  is the thermal conductivity of the solid,  $\rho$  is its density and  $c_p$  the specific heat of the solid material. Eq. 4.1 is obtained from the energy balance equation combined with Fourier's conduction law

$$Q = -K \frac{\partial T}{\partial x}, \quad (4.3)$$

which relates the energy flow with the temperature gradient. The boundary conditions are:

$t \geq 0, x = 0, Q(\text{heat flux}) = P_0$  (beam power density, assumed constant). The solution of Eq. 4.1 with these boundary conditions is [26]:

$$T = \frac{P_0}{K} \int_x^\infty \operatorname{erfc} \frac{x}{2\sqrt{\kappa t}} dx, \quad (4.4)$$



which relates the temperature to the power density. The temperature at  $x = 0$  is given by

$$T(x = 0) = \frac{2P_0}{K} \left( \frac{\kappa t}{\pi} \right)^{\frac{1}{2}}. \quad (4.5)$$

Using the semi-infinite solid approximation, the heat penetration depth/length,  $\lambda$ , for a beam pulse duration  $\tau_p$  can be estimated through [26]:

$$\lambda = \left[ \left( \frac{K}{c_p \cdot \rho} \right) \tau_p \right]^{\frac{1}{2}}, \quad (4.6)$$

and the penetration time through the plate thickness  $d$  can be estimated as:

$$\tau = \frac{d^2}{\left[ \frac{K}{c_p \rho} \right]} \gg \tau_p. \quad (4.7)$$

The approximation is valid when the following conditions are met:

- the penetration length,  $\lambda$ , is much shorter than the target plate thickness,  $d$  (that is,  $\lambda \ll d$ ).
- the penetration time,  $\tau$ , is much longer than the pulse length,  $\tau_p$  (that is,  $\tau \gg \tau_p$ ).

The Beam Stop is made of Carbon-Fibre-Composite (CF222-Shunk Intec S.L.), an anisotropic material with favourable in-plane conductivity. The Target Calorimeter is made of CFC Carbon (CX-1001U), a highly anisotropic material with the higher conductivity perpendicular to the plane. The thermal constants of both materials are shown in Tab. 4.1 below. For either targets, the penetration times and lengths satisfy the semi-infinite solid approximation requirements for heat propagation in the assumed directions.

Property	Composite CX-1001U(TC)	Composite CF222(BS)
Conductivity, $K$ (W/cm/K),	0.3 $\parallel$ and 6.7 $\perp$	0.8 $\parallel$ and 0.25 $\perp$
Density, $\rho$ (g/cm <sup>3</sup> )	1.9	1.8
Specific heat, $c$ (J/g/K)	0.75 (at 100 °C)	1.635 (at $\sim$ 600 °C)
Plate thickness, $d$ (mm)	15	12
Penetration length in 100 ms (mm)	1.5 $\parallel$ and 6.9 $\perp$	1.6 $\parallel$ and 0.9 $\perp$
Penetration time for plate thickness (s)	10.69 $\parallel$ and 0.48 $\perp$	5.3 $\parallel$ and 16.95 $\perp$

TABLE 4.1: Material properties with the parallel ( $\parallel$ ) and perpendicular ( $\perp$ ) thermal constants for the Target Calorimeter (Composite CX-1001U) and Beam Stop (Composite CF222).

The thermal constants of copper, and the characteristic times for heat conduction and heat radiation are shown on Tab. 4.2. The penetration time, 3.5 s

is much longer than the pulse length ( $< 0.2$  s), whereas the penetration depth is 3.3 mm ( $\ll 20$  mm). These both satisfy the semi-infinite solid approximation, which will be used in the interpretation of the calorimetric measurements at the V-calorimeter.

Property	$\rho$ (g/cm <sup>3</sup> )	$c$ (J/g/K)	$K$ (W/cm/K)	Plate thickness (mm $\times$ mm $\times$ mm)	$\lambda$ (100 ms) (mm)	$\tau_{cond.}$ (s)	$\tau_{rad.}$ (h)
Copper	8.93	0.386	3.94	750 $\times$ 330 $\times$ 20	3.3	3.5	2

TABLE 4.2: Thermal constants of copper, and the characteristic times for heat conduction and radiation.

Since the required conditions for the semi-infinite approximation are fulfilled for each of the graphite targets in the assumed direction of heat conduction, the temperature recorded can be related with the incident power through a simple equation. The temperature map of the target plate can then be transformed into the incident beam power density map, and therefore power density contours and profiles of the beam can be obtained.

The different diagnostics are explained below.

## 4.2 Water calorimetry at the ‘V-calorimeter’

The V-calorimeter, so-called because of its V-shape, is positioned at the entrance to the beam duct and it intercepts the full beam cross section transmitted from the neutralization chamber at the exit of the “Ion removal system” (Fig. 4.2). The calorimeter serves a dual purpose: to obtain a measurement of the beam power upstream of the drift duct, and as beam target during the long conditioning periods, allowing for beam optimization by adjusting the different parameters that determine the beam formation such as the gas, Arc voltage, and the magnet current- to obtain the desired beam parameters.

It is made up of two water-cooled copper plates of 20 mm thickness, arranged in a fixed “V-shape” with the vertical apex facing away from the beam [27].

The V-shaped construction results in a reduction of the peak incident power density from 20 MW/m<sup>2</sup> to below 10 MW/m<sup>2</sup> [28]. Assuming a peak flux of 20 MW/m<sup>2</sup>, the calorimeter was designed to handle 30 MW/m<sup>2</sup> peak power density normal to the copper plate, for 0.5 s beam pulse every 10 s. The total power intercepted was assumed to be 2 MW.

The incident beam’s energy is deposited on the copper surface, and the heat generated is propagated through the plate thickness by heat conduction. The heat penetration depth for a pulse length of 100 ms is 3.3 mm, which is small compared with the plate thickness (20 mm). The penetration time (the time required for the heat to penetrate the whole thickness of the plate) is 3.5 s, which is much longer than the pulse length (0.2 s). Temperature uniformization through the plate thickness occurs long after the beam pulse has ended.

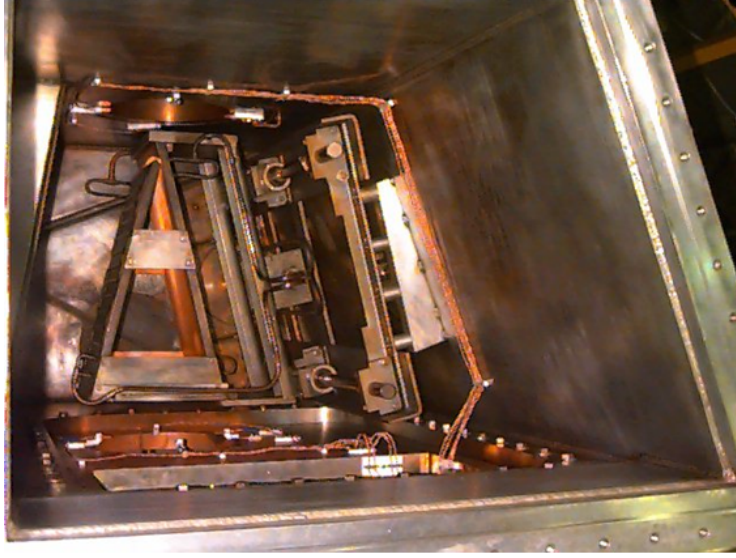


FIGURE 4.2: V-calorimeter in its position as seen from above a diagnostic port of the TJ-II.

The plates radiate heat according to the Stefan-Boltzmann law:

$$c \cdot \rho \cdot V \cdot \frac{dT}{dt} = -\epsilon \cdot \sigma \cdot S \cdot (T^4 - T_R^4) \quad (4.8)$$

where  $\epsilon$  is the emission coefficient,  $\sigma$  is Boltzmann’s constant ( $5.67 \times 10^{-8} \text{ Wm}^{-2}\text{K}^{-4}$ ) and  $T_R$  the radiation temperature (K). The estimated time needed for radiative cooling is 2 hours. The thermal constants of copper, and the characteristic times of heat conduction and heat radiation for the V-calorimeter are summarised in Tab. 4.2.

Since the penetration time is longer than the pulse length, the plates must be cooled down between the pulses, which corresponds to what is described as “inertial cooling”. The plate cooling is achieved by means of 10 mm diameter cooling pipes made of copper, welded on the back side of the plates. The circulating water removes the heat from the plates in a time that ranges between 2 and 3 minutes, depending on the water flow. On the other hand, the 2 hours necessary to cool down the plates by radiative cooling is very long compared with the beam pulse length and the water cooling energy removal time. The energy deposition and removal from the V-calorimeter can therefore be considered as adiabatic processes. All the beam energy ends up in the water circulating through the cooling pipes.

The energy intercepted by the V-calorimeter can be obtained from the temperature difference between the water inlet and outlet, and the water flow, according to the expression:

$$E_{water} = \int c_w \cdot \rho \cdot Q \cdot \Delta T \cdot dt \quad (4.9)$$

where  $c_w$  = specific heat of water [J/kg.K],  
 $\rho$  = density of water [kg/m<sup>3</sup>],

$Q$  = volumetric flow of water [ $\text{m}^3/\text{s}$ ], and

$\Delta T$  = temperature difference between inlet and outlet [ $^\circ\text{C}$ ].

The temperature difference in the water is measured by a thermopile instrument, using 20 thermocouple joints in series, in thermal contact with the inlet and outlet pipes to the calorimeter plates. There is a separate circuit for each of the two calorimeter plates (left and right).

Time integration of the  $\Delta T$  traces yields the beam energy through the expression in Eq. 4.9, when all the constant magnitudes are taken into account. The  $\Delta T$  measuring instruments are manufactured by the “Delta-T” company. Their main characteristics are listed below.

Sensitivity	0.4 mV/ $^\circ\text{C}$
Accuracy	$\pm 0.12^\circ\text{C}$
Dynamic response	$< 0.5 \text{ s}$
Calibration factor (after amplification $\times 1000$ )	$0.4 \text{ V}/^\circ\text{C} + / - 2 \% \text{ max}$

TABLE 4.3: The Delta T measuring device characteristics.

The water flow is measured with turbine type flow meters of the “Flow Technology” company, model FT 6–8. The instrument main characteristics are given in the Tab. 4.4 below.

Flow range	1.9–19 l/min
Repetitivity	$\pm 0.05 \%$
Linearity	$\pm 0.5 \%$
Dynamic response	10 ms (square waveform)

TABLE 4.4: Water flow measuring device characteristics.

In Fig. 4.3 the time traces from the measurements for a typical beam pulse are shown.  $\Delta T$  reaches a maximum after around 4–5 s, after which a steady decay is observed for approximately 2.5 minutes until  $\Delta T = 0$  is reached.

Perveance scans are done according to the relation in Eq. 2.6, and are therefore achieved in two ways: energy scans (varying  $V$ ) and current scans (varying  $I$ ).

In the energy scans, the beam acceleration voltage,  $V_{\text{accel}}$ , measured between the plasma electrode and the Earth electrode of the grid system, is varied (at constant  $I_{\text{accel}}$ ) whereas the current scans are achieved by varying the beam extraction current,  $I_{\text{accel}}$ , which is done by changing the Arc voltage between the anode and the cathode of the plasma source.

In both scans, the ion source power ( $P_{\text{elec}}$ ) and the beam power deposited on the V-calorimeter with bending magnet ON ( $P_{V\text{cal},BM}$ ), and without bending magnet ( $P_{V\text{cal},NoBM}$ ), are measured and recorded. The power deposited on the calorimeter,  $P_{\text{cal}}$ , is directly measured by water calorimetry:  $P_{V\text{cal}} = E_{\text{water}}/\tau_p$ .

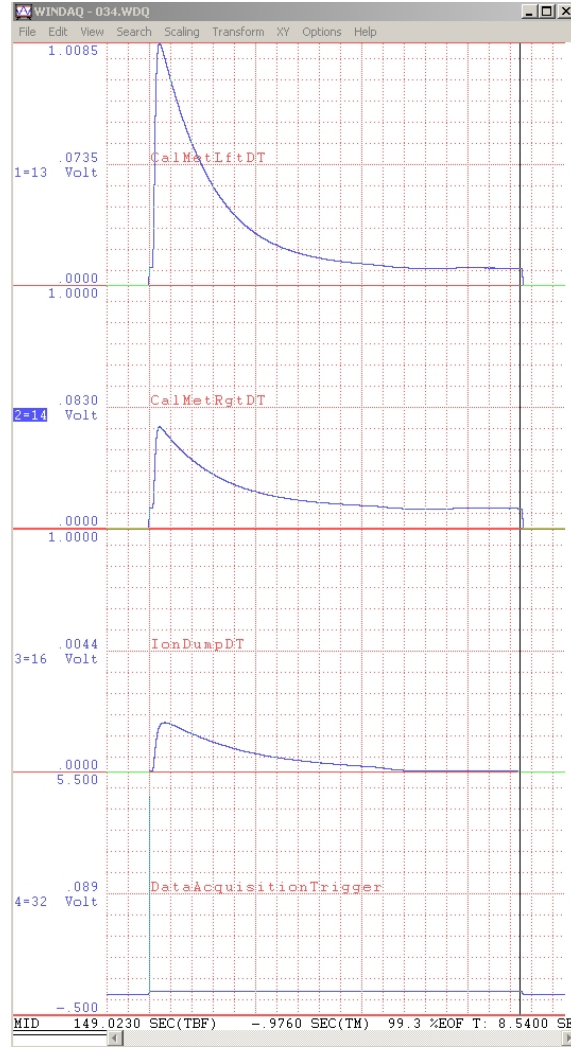


FIGURE 4.3: Time traces of the  $\Delta T$  signal used in calorimetric measurements for a typical beam pulse.

$P_{elec}$  is obtained from the electrical measurements:

$$P_{elec} = I_{accel} \times V_{accel}, \quad (4.10)$$

and the beam perveance is determined using  $I_{accel}$  and  $V_{accel}$  according to the expression in Eq. 2.6.

The beam’s transmission and neutralization fraction measurements are done on the V-calorimeter.

The power transmission is the ratio of the full beam power intercepted by the calorimeter with the bending magnet OFF (due to neutrals plus ions) to the extracted beam power at the ion source  $P_{elec}$ . By water calorimetry at the V-calorimeter, the geometrical power transmission is measured by comparing the beam power deposited on the calorimeter with the bending magnet OFF,  $P_{Vcal, NoBM}$ , to the beam power at the neutralizer entrance (given by the ion

source power),  $P_{elec}$ . Geometrical transmission (%)

$$= \frac{P_{Vcal, NoBM}}{P_{elec}} \times 100. \quad (4.11)$$

The neutralization fraction is estimated by comparing the beam power deposited on the V-calorimeter with the bending magnet ON,  $P_{Vcal, BM}$ , to the case with the bending magnet OFF,  $P_{Vcal, NoBM}$ . Neutralization fraction  $F$  (%)

$$= \frac{P_{Vcal, BM}}{P_{Vcal, NoBM}} \times 100 \quad (4.12)$$

### 4.3 Infrared (IR) Thermography Principle

Infrared thermography was used to monitor the temperature of two different targets inside TJ-II vessel [10, 29, 30].

Infrared (IR) thermography exploits the principle of black body radiation and the fact that a body capable of absorbing all radiation at any wavelength is equally capable of emitting the radiation (Kirchhoff's law of black body radiation). It makes use of the infrared spectral band, spanning the infrared wavelengths not less than 1.2 micrometres (in the range 1.2–100 microns). A body's emissivity describes the fraction of the radiant emittance of a black body produced by that body at a given temperature.

The spectral distribution from a black body is described by Planck's law (Eq. 4.13). Spectral radiant emittance ( $W_{\lambda_b} \text{ Wsr}^{-1}\text{m}^{-3}$ ) at wavelength  $\lambda$  (m) is

$$W_{\lambda_b}(\lambda, T) = \frac{2hc^2}{\lambda^5} \frac{1}{e^{\frac{hc}{\lambda k_B T}} - 1}, \quad (4.13)$$

where  $c$  is the velocity of light ( $3.0 \times 10^8 \text{ ms}^{-1}$ ),  $h$  is Planck's constant ( $6.62 \times 10^{-34} \text{ Js}$ ), and  $k_B$  Boltzmann's constant ( $1.38 \times 10^{-23} \text{ JK}^{-1}$ ). The total radiant emittance  $W_{\lambda_b}$  is described by the Stefan-Boltzmann law (Eq. 4.14), that relates the total emissive power of a black body and its absolute temperature  $T$  (K).

$$W_b = \sigma T^4, \quad (4.14)$$

where  $\sigma$  is Stefan-Boltzmann constant ( $5.67 \times 10^{-8} \text{ Wm}^{-2}\text{K}^{-4}$ ).

The Target calorimeter and Beam Stop target used in this thermographic diagnostics are opaque material targets with zero transmittance, but they do not act exactly like black bodies (are grey) since a fraction of the incident radiation may be reflected. The total emissive power is a fraction  $\epsilon$  ( $< 1$ ) of that of a black body at the same temperature, with total emittance  $W$  described by

$$W = \epsilon \sigma T^4 \quad (4.15)$$

where  $\epsilon$  is the characteristic emissivity of the material, that is a function of temperature and detection angle.

## 4.4 IR Cameras

In the thermography of the targets, cameras were used to view the targets. The Infrared-type of cameras were of particular interest, since we are working with light emission in the Infrared range of the electromagnetic spectrum. It is important that a good choice is made in the design of the infrared camera lens: the lens should be of high refractive index and good IR transmittance.

Common infrared transmitting materials that can be used for the Infrared camera lens design include Germanium (*Ge*), Silicon (*Si*), Arsenic Trisulphide glass (*As<sub>5</sub>S<sub>3</sub>*), Irtran 2 (*ZnS*), Sapphire (*Al<sub>2</sub>O<sub>3</sub>*) and Irtran 1 (*MgF<sub>2</sub>*). Since materials with high refractive indices have low transmittances, the transmittances are usually increased by use of anti-reflection coatings.

The infrared camera used on the Target Calorimeter is an OPTRIS PI 160 camera. Its lens has angular aperture of  $23^\circ \times 17^\circ$  and a minimum focal distance of 0.2 m. The camera specifications are summarized in Tab. 4.5. The personal computer (PC) compatible software OPTRIS was used to perform remote control of the camera, as well as thermographic analysis and image treatment. The interface between the IR camera in the stellarator hall and the PC in the NBI control room is made through a pair of custom-made positive emitter coupled logic (PECL) optical fibre transmitters and a parallel interface PI500/900 [10, 30].

Spectral range	7.5–13 mm
Detector UFPA	$160 \times 120$ pixels
Lens Field of Vision (FOV)	$230 \times 170$
Temperature ranges	$-20 \dots 100^\circ\text{C}$ ; $0 \dots 250^\circ\text{C}$ ; $120 \dots 900^\circ\text{C}$
System accuracy	$\pm 2^\circ\text{C}$ or $\pm 2\%$
Temperature resolution (NETD)	0.08 K with $23^\circ\text{C}$
Frame rate PI160	120 Hz

TABLE 4.5: Optical specifications for the OPTRIS PI 160 camera.

To view the targets, the camera was in each case set to capture images through an infrared window incorporated in the lower part of the duct (see Fig. 4.5) allowing a line of sight along the beam axis. Due to its proximity to the camera (500 mm), the Target Calorimeter cannot be visualized in full, and the effective dimensions of the infrared window, 130 mm  $\times$  23 mm, further limit the field of vision in the vertical dimension. Besides, due to mechanical constraints in the duct area the camera cannot be placed as close to the window as necessary, therefore the infrared image of the target is reflected onto a steerable IR mirror for the TC measurements, allowing a vertical alignment of the camera.

The visual field depends strongly on the mirror orientation, and a change of inclination by  $1^\circ$  shifts the sight of the target by 50 mm [30]. The dimensions

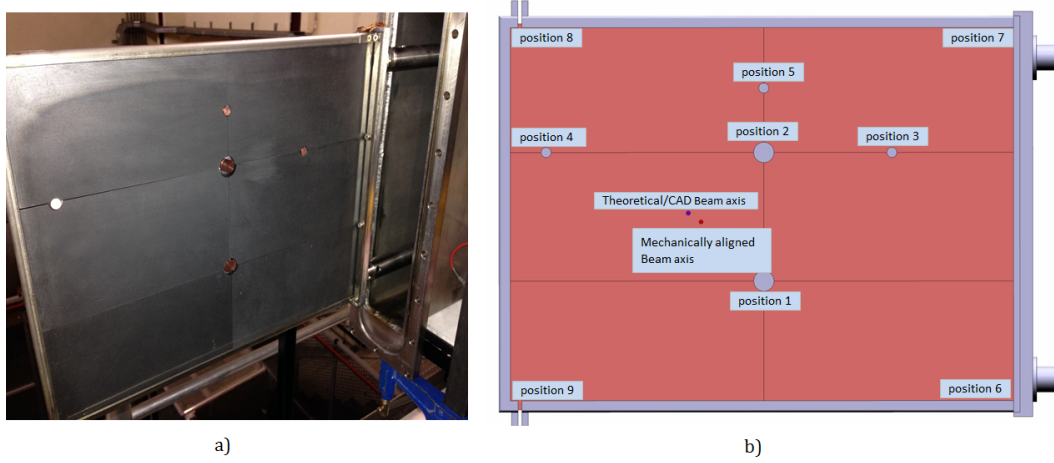


FIGURE 4.4: Photograph of TC showing the copper buttons (a), and the CAD drawing of the TC showing the position of the copper buttons (1, 2, 3, 4, and 5) and the beam axis - theoretical and mechanically determined beam axes (b).

of the target and its distance to the virtual observer give images a distorted appearance due to perspective effects. Besides acting as field diaphragm, the infrared window functions as aperture diaphragm in the vertical direction, limiting the illumination of the image for target areas at large viewing angles.

The choice of the window material is such that it is transparent to the infrared light. The window is a 5 mm thick rectangular plate of barium fluoride ( $\text{BaF}_2$ ),  $65 \times 145 \text{ mm}^2$  in dimension. The stellarator vacuum side has a protective shutter installed in it, to shield the IR window during glow discharge cleaning of the machine. The nominal transmittance of the barium fluoride is 92 % in all the spectral range between 0.2 and  $11 \mu\text{m}$ .

The infrared mirror is a commercially available plate of fused silica substrate  $133 \times 70 \times 10 \text{ mm}^3$  in dimension, with a gold coating of 98 % reflectivity between 7.5 and  $11 \mu\text{m}$ . The mirror is mounted on a movable frame to allow for rotation around a horizontal axis and parallel displacement [29]. For the BS measurements, the camera's field of view includes the BS position and therefore direct viewing is possible without the mirror.

## 4.5 The Target Calorimeter

### 4.5.1 IR images as thermal prints of the beam

Infrared thermography on the Target Calorimeter (TC) enables us to study the power density distribution of the neutral beams. The Target Calorimeter is a  $400 \times 300 \text{ mm}^2$  rectangular target made up of six  $200 \times 100 \text{ mm}^2$  CX-1001U Carbon-Fibre-Composite (CFC) [24] plates of 15 mm thickness mounted on a stainless steel frame. It is positioned at a distance of 4,541.5 mm from the ion source. The plates are fixed in position by two copper buttons.



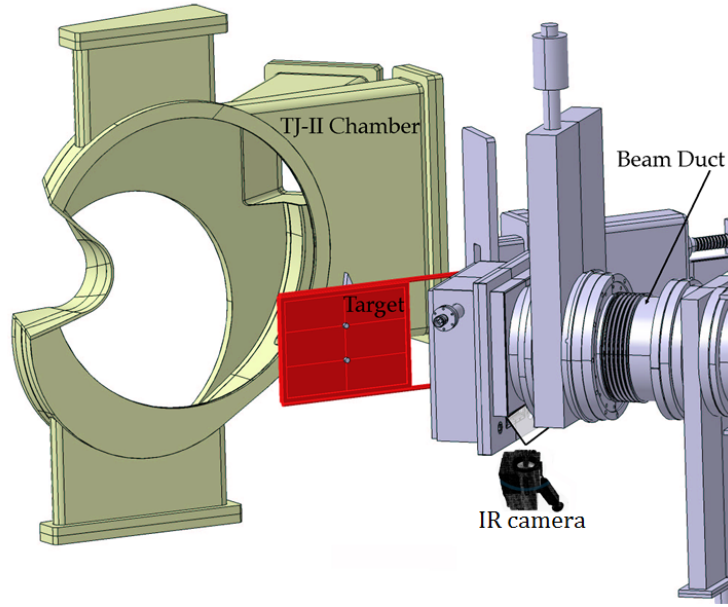


FIGURE 4.5: CAD view of the target calorimeter in working position at TJ-II. A sector of the machine is removed from the drawing to better show the target calorimeter (TC) arrangement and its relative position with respect to the IR window, mirror, and camera [10, 29, 30, 31].

The graphite plates have been machined to house the button heads screwed in their inner corners. The copper screws act as both plate supports and adiabatic thermal probes for calibration purposes. In the back of the screws are embedded two type E thermocouples, from which the temperature of the copper can be obtained with a time constant of several seconds and from which the power density of the beam can be pinned down at two points on the target. Three additional copper buttons are positioned between neighbouring plates, that serve as fixed reference points for image reconstruction. Fig. 4.4 shows a photograph of the Target Calorimeter and a CAD drawing showing the location of the copper buttons.

The TC material is CX-1001U Carbon-Fibre-Composite (CFC) [24], especially chosen due to its highly anisotropic thermal conductivity. The woven fabric in the CX-1001U CFC material of the target is grown perpendicular to the plate plane, resulting in highly anisotropic thermal properties (see Tab. 4.1 for details): the thermal conductivity at room temperature is  $670 \text{ W m}^{-1} \text{ K}^{-1}$  perpendicular to the plane (parallel to the woven fabric), over 20 times higher than the in-plane propagation conductivity which is only  $30 \text{ W m}^{-1} \text{ K}^{-1}$ . The underlying principle of using the Target Calorimeter is that the thermal print of the pulsed neutral beam (100 ms) on the target reflects as accurately as possible the power density distribution of the beam [32]. The short pulse length (100 ms) allows the use of the semi-infinite plate approximation to estimate the time constants for temperature uniformization, which have been

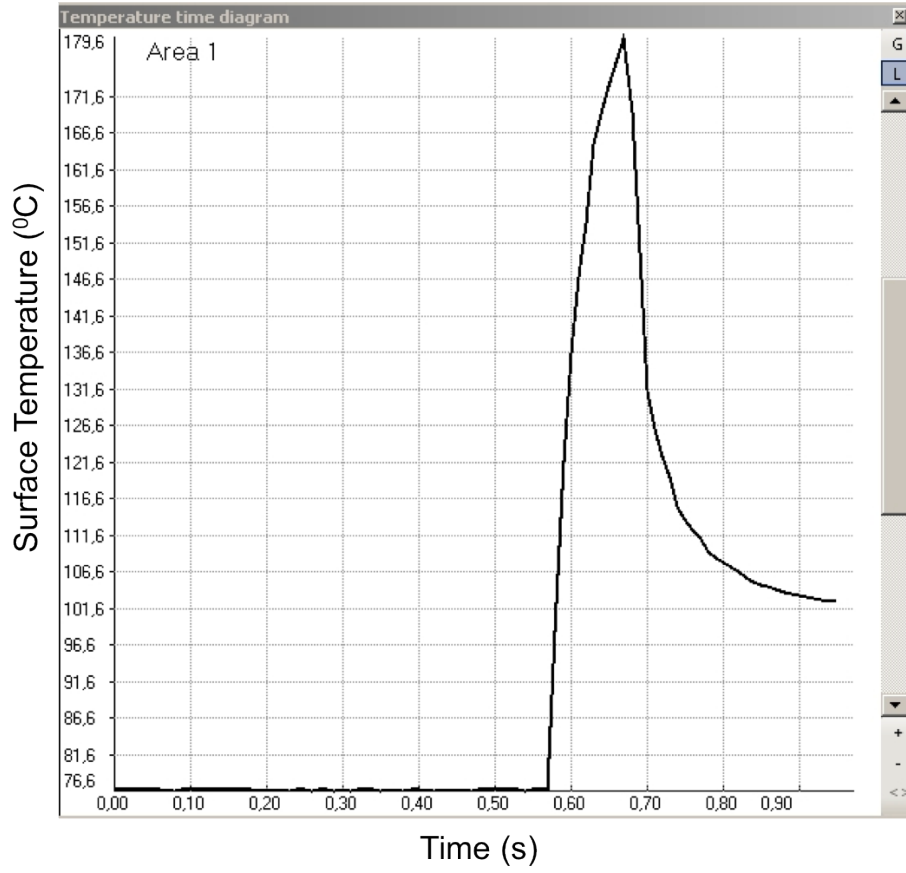


FIGURE 4.6: Time trace of the surface temperature of the graphite plate at the location of maximum  $T$ .

experimentally confirmed by the surface temperature evolution of a spot on the target observed with the infrared camera. Fig. 4.6 shows the time trace of the surface temperature at the location of the maximum  $T$  on the graphite plate. The time constant for the temperature to become uniform is 0.5s in the perpendicular direction and 13s for in-plane heat propagation, and the estimated time constant for radiation cooling is three orders of magnitude higher than the pulse length, which means that for several seconds after the pulse the thermal print of the beam on the target closely portrays the power density distribution of the beam.

The infrared image of the target is captured during and after the beam pulse and the target temperature distribution, as measured by the IR camera, is a mimic of the neutral beam power density distribution [29, 31, 30].

The aim of this study is to obtain the beam power density profiles from infrared images such as that in Fig. 4.7. As expected from this kind of heating neutral beams, the temperature distribution should be fitted to a Gaussian beam profile to a good approximation, as given by Eq. 2.7 [13].

From the resulting Gaussian profiles, the  $1/e$  divergence angle,  $\theta_{1/e}$ , can be determined using  $a = d \cdot \tan \theta_{1/e}$  and their dependencies on the beam perveance,

can be got for different beam parameters. In this case  $d = 454.15$  cm and the  $1/e$  widths are determined from the Gaussian fit results.

Obtaining Temperature profiles from the IR images involves two different tasks: the transformation of coordinates from Image Coordinates (IC) to real coordinates, and the calibration of the graphite temperatures.

Fig. 4.7 shows two IR images of the TC. On the left is shown the thermographic image of the TC before arrival of the beam. It has a very inhomogeneous appearance, due to differences in the emissivities of the different plates. On the right, the IR image 0.5 s after the pulse has a homogeneous appearance, after the initial image has been subtracted. Only subtracted images will be used in the analysis.

In the left image, the lines marking the edges of the plates show a large inclination angle, and do not appear parallel. They correspond to horizontal and vertical lines in real coordinates, but due to the proximity of the TC to the camera lens, the image coordinates are greatly distorted. The analysis of the IR images requires a transformation of coordinates from Image Coordinates (IC) to real coordinates. This kind of conversion can be treated as a “Projective Transformation”.

The graphite temperature as measured by the IR camera depends on the emissivity of the surface and the transmissivity of the window. The apparatus and materials were independently calibrated to match the emissivity of the target material, the transmittance of the IR window, the ambient temperature, the atmospheric temperature and humidity [29]. Nevertheless, the graphite emissivity evolves along the experimental campaign due to deposition of elements present in the plasma environment, and the transmissivity of the BaF<sub>2</sub> window is degraded for the same reasons. To overcome these uncertainties, the temperature measurement of two copper buttons on the CFC plate is used. The buttons are mounted with good thermal insulation from the surrounding plates, so they behave as adiabatic calorimeters with respect to the intercepted beam power: the temperature increment of each button after a beam pulse is a direct measurement of the intercepted power. Surface temperatures can be directly converted to power density, without the need of an absolute calibration for the graphite temperature [30, 29, 31].

### 4.5.2 Transformation from Image Coordinates to Real Coordinates

To illustrate the need of a correct conversion of the image coordinates, the two straight lines drawn on the images of Fig. 4.7 correspond to horizontal and vertical lines in real space. To obtain a horizontal beam profile, the horizontal line through the temperature maximum must be first converted to Image Coordinates. The software of the camera can then produce the temperature profile in image coordinates, that must be converted to real coordinates for profile analysis.

The Image Coordinate system (IC) is a matrix of 160 points in horizontal di-

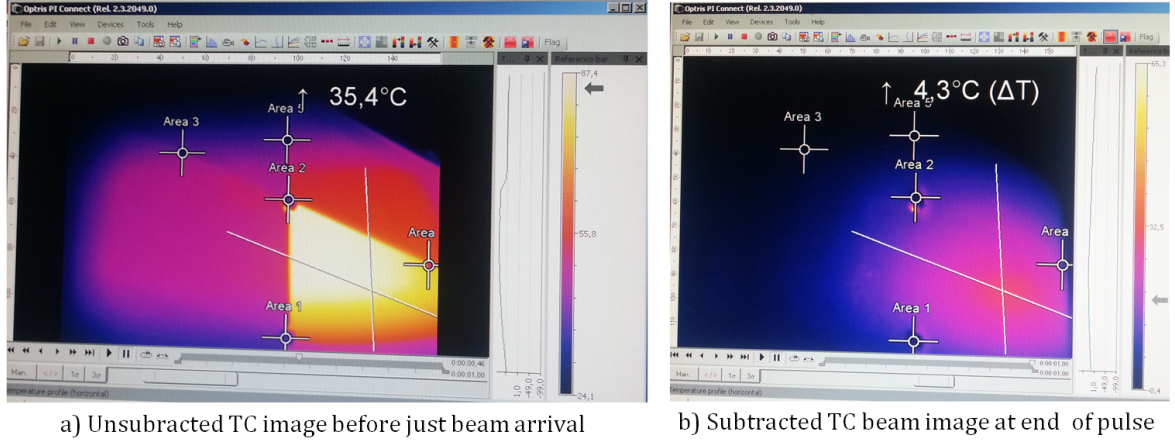


FIGURE 4.7: Target Calorimeter images. a) Un-subtracted image of TC, b) Subtracted image of TC at the end of the pulse. The two lines for generating the profiles are shown.

rection and 120 points in vertical direction. It describes the position of a pixel as a set of two coordinates  $(X, Y)$  that are integer numbers counted from the upper left corner of the image.

As real coordinate system we have chosen the “Beam Coordinate system” (BC) described in Tab. 4.6. For the coordinate conversion between IC and BC two

Origin	intersection of the beam nominal axis with the injection port plane
X-axis	horizontal with $X > 0$ to the left looking in the beam direction
Y-axis	vertical with $Y > 0$ upwards
Z-axis	beam axis, horizontal with $Z > 0$ towards TJ-II

TABLE 4.6: Beam Coordinates.

complementary tools are used:

- An Excel Macro allows conversion on a point by point basis [33]. This approach is used to find the line in IC corresponding to a horizontal (or vertical) line in BC.
- A Matlab script is used to convert the points on a line in IC to BC. To build the transformation matrix of the projective transformation the script needs as input the coordinates in BC and IC systems of at least four non-colinear points in the image [34].

The positions of the five copper buttons on the Target have been used. The Beam coordinates of those points are fixed, independent of the optical alignment of the camera. The Image coordinates of the five buttons vary nonetheless with the mirror angle, camera position, and any change in the system alignment. In Fig. 4.7 the positions of the five buttons are marked.

To obtain the power density profile in Beam Coordinates, the following procedures were used (see appendix 1 for details).

1. Image subtraction: Since our interest is in the temperature change on the target due to the beam, the infrared thermal image of the Target Calorimeter, which is horizontally inverted, was first subtracted (to eliminate the effects of any initial temperatures of the target before the beam's arrival) using the OPTRIS PI 160 camera software. This was done for each of the TC thermographic images captured during perveance scans done on the TC, and in each case only the last frame (at time,  $t = 1.0$  s) was considered in the analysis, which is 0.5 seconds after the beam pulse.
2. Tmax location on the image: The maximum temperature on the plate was determined, and its position in Image co-ordinates noted.
3. Tmax location in Beam coordinates: Using the Excel Macro which was specifically written for this purpose, the co-ordinates of the temperature maximum point were transformed to Beamline coordinates.
4. Horizontal line in Beam coordinates: Two extreme points on opposite sides of the maximum define a horizontal line.
5. Horizontal line in IC: The two extreme points are transformed back to Image co-ordinates using the Excel Macro.
6. Horizontal profile in IC: These two lines are used to generate the required profiles through the point of maximum temperature using the camera software (OPTRIS).
7. Horizontal profile in BC: The positions of the five buttons in IC are given as input to generate the transformation matrix. The IC profile coordinates are fed to the Matlab script (the IC profile is given as input.) The output of the script is the converted horizontal profile in BC.

### 4.5.3 Measurement of beam power density at two localized points on the Target

Due to the thermal properties of the CFC material, the temperature map until 10 s after the beam pulse is proportional to the beam power density distribution on the target plane. But there are uncertainties related to the temperature reading with the infrared camera that preclude the direct conversion from temperature to power density. A way to overcome these uncertainties is to directly determine the power density at certain locations using the temperature rise of adiabatic calorimeters, such as the copper buttons.

The buttons have been shown to have a nearly perfect adiabatic behaviour [30, 31]. They are therefore used to find the relation between graphite plate temperature  $\Delta T_g$  (measured from the IR thermography) and the incident beam

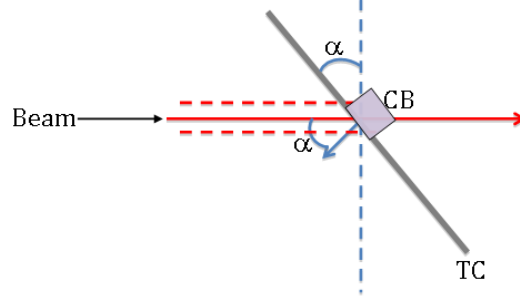


FIGURE 4.8: Illustration of incident beam and copper button (CB) on target calorimeter (TC) geometry, as used to determine the incident power density  $p_0$  on CB.

power density  $p_0$  from the temperature readings of the thermocouples embedded in the two copper buttons.

To determine this relationship, the incident power density on the Copper button is calculated as  $p_{CB} = E_{CB}/\Delta t$ , where  $E_{CB}$  is the energy deposited on the copper button by the beam and  $\Delta t$  is the pulse duration (0.1 s).  $E_{CB}$  is obtained from the thermocouple measurements as:

$$E_{CB} = m_{CB} \cdot c_{Cu} \cdot \Delta T_{CB}. \quad (4.16)$$

Here, the mass of the copper button is  $m_{CB} = 7.4$  g,  $c_{Cu}$  is the specific heat of copper and  $\Delta T_{CB}$  is the temperature change measured by thermocouple.

In Fig. 4.8, the direction of the incident beam is shown to make an angle  $\alpha = 45^\circ$  with the Target plane (and the Copper button surface).

The beam power  $p_{CB}$  intercepted by Copper Button is

$$p_{CB} = E_{H^0} \cdot j_{perp.}^{H^0} \cdot S_{CB} \cos \alpha, \quad (4.17)$$

with the kinetic energy of a neutral beam atom  $E_{H^0} = mv_B^2/2$ , number of  $H^0$  atoms per unit surface perpendicular to the beam per unit time  $j_{perp.}^{H^0}$ , perpendicular beam surface intercepted by the button  $S_{CB} \cos \alpha$  and power per unit surface perpendicular to the beam  $p_0^{CB} = E_{H^0} \cdot j_{perp.}^{H^0}$ .

The infrared temperature of the graphite  $\Delta T_g$  at the Copper Button (CB) position is taken as that of the isotherm passing through the CB position. It is determined by interpolating at the CB position, the temperature profile that crosses the Tmax point and the CB position. This interpolated temperature corresponds to the incident power density.

At any other point on the TC the relationship between beam power density and TC surface temperature is the same.

The power density  $p_0^{CB}$  at the copper buttons has been estimated for several beam parameters of the perveance scan (different profiles and beam power values) and the corresponding interpolated  $\Delta T_g$  in the graphite have been obtained. The results corresponding to the copper button 2 are represented in Fig. 4.9. A linear relationship between incident power density and graphite

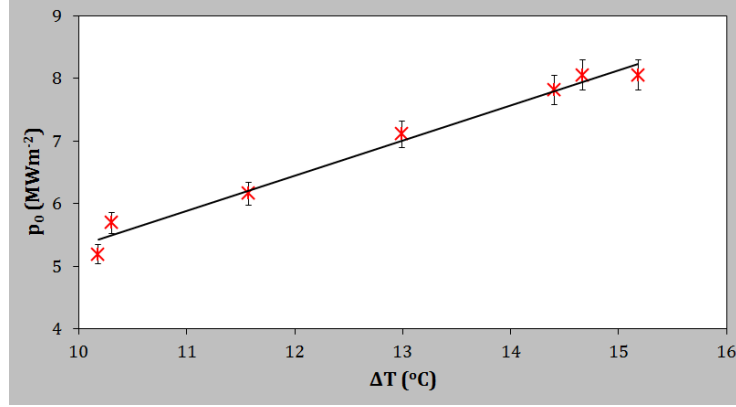


FIGURE 4.9: Relation between incident power density  $p_0$  on copper button 2 and Infrared thermographic temperature  $\Delta T_g$  of the CFC graphite plate.

temperature is observed, as expected.

The plot in Fig. 4.9 shows the linear relation of  $p_0$  and  $\Delta T_g$  which is given by

$$p_0 \text{ (MWm}^{-2}\text{)} = 0.5616\Delta T_g \text{ (}^\circ\text{C)} - 0.2982. \quad (4.18)$$

Unfortunately, this relationship could not be confirmed for the lower copper button. The linearity exists, but the infrared temperature reading is greatly undervalued, due to the limiting effect of the port bottom wall and the window lower edge. Slight variations in the optical alignment greatly affect the apparent temperature, which is not the case in the plate region near the upper copper button.

For this same reason, the temperature vertical profiles are not considered in the beam divergence analysis. The horizontal profile on the other hand is not affected by the window Field of View restriction.

## 4.6 The Beam Stop Target

To monitor the re-ionization losses in the vacuum chamber, infrared images of the Beam Stop target positioned at the beam exit are used. In Fig. 4.10, a horizontal section of TJ-II and NBI-1 shows the location of the protecting graphite plates at the duct and the BS target. The Beam Stop target is positioned 6.4635 m from the ion source.

The Beam Stop is a target plate made from Carbon-Fibre-Composite (CF222-Shunk Intec S.L.) material. The fibres of the CFC material are oriented along the plane. The thermal and material properties of the target plate are summarised in Tab. 4.1. For a 100 ms pulse, the in-plane propagation length is less than 2 mm which is below the spatial resolution of the IR camera (i.e. 3.2 mm) for objects at a distance of 2.5 m. Therefore, we can consider the target to be ideally represented by a semi-infinite solid whose surface is hit by a constant and uniform power flow, such that for 100 ms beam pulses the surface temperature rise of the plate can be assumed to be proportional to the incident



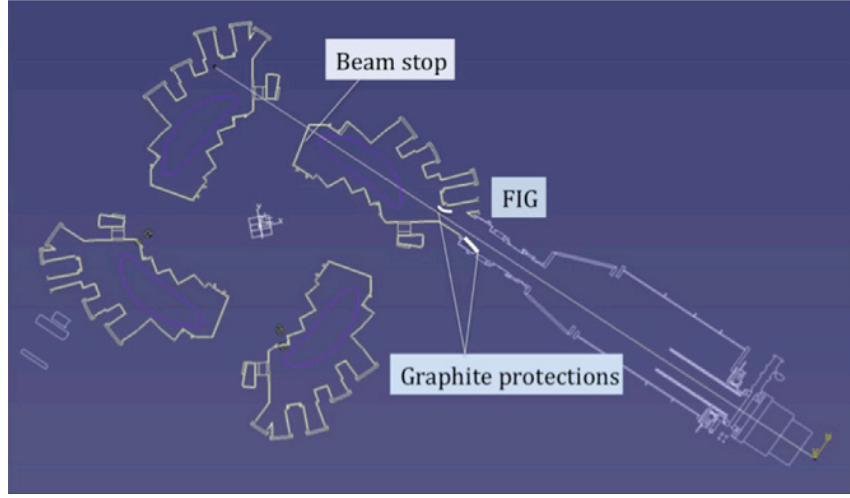


FIGURE 4.10: CAD rendering of the horizontal section along NBI-1 beam axis, showing TJ-II vessel, NBI-1 beamline and duct, and BS position in TJ-II [10].

power density.

In Fig. 4.11a., an infrared image recorded after a 100 ms beam pulse with no magnetic field is presented. The image is left-right inverted due to the camera alignment. The camera aims directly at the beam stop, the Field of View in this arrangement includes the Beam Stop in full, and no mirror is needed. The surfaces directly hit by the beam are shown: the graphite protection of the TF coil appears out of focus to the left (right), whereas the stainless steel plates covering the central coils and the graphite beam stop are in focus in the image centre.

When the temperature profiles are studied both with TJ-II  $\vec{B}$  field ON and OFF, the re-ionization losses are estimated. With the  $\vec{B}$  field OFF, the full beam power (neutrals plus ions),  $P_{neut.+ions}$  reaches the target. With the TJ-II  $\vec{B}$  field, the ions born in the duct and TJ-II entrance through collisions with the residual gas, are deflected before encountering the last closed magnetic surface and do not reach the target [35]. The beam power  $P_{neut.}$  that reaches the beam stop plate is reduced with respect to the case when NO  $\vec{B}$  field is present. Neglecting the fraction of ions born inside the last magnetic surface (that are confined by the magnetic field), the fraction  $P_{neut.}/P_{neut.+ions}$  can be taken as a measure of the transmitted power, from which the re-ionization fraction  $F_r$  can be obtained.

Therefore, by comparing infrared images of the Beam Stop plate for pulses with, and without TJ-II  $\vec{B}$ -field, the re-ionization fraction can be estimated. The temperature rise during the pulse,  $\Delta T_B$ , at any point on the BS plate is proportional to the local power density where

$$\Delta T_B = T_{t=100} - T_{t=0}. \quad (4.19)$$



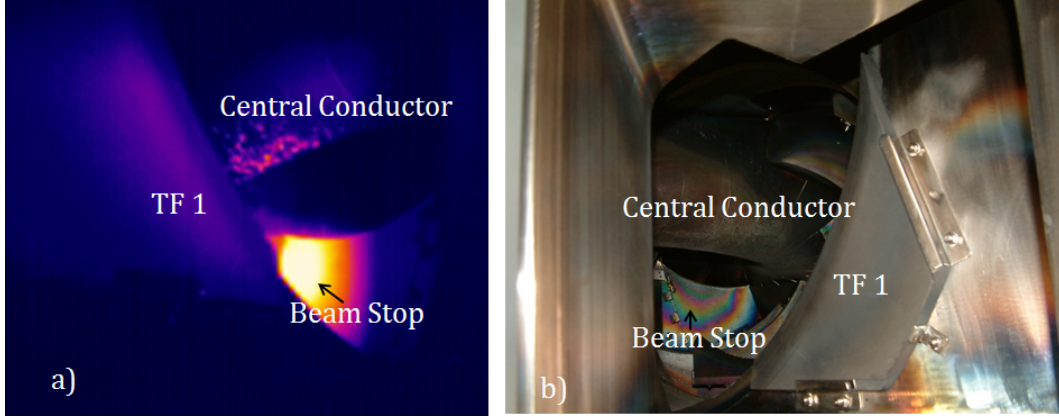


FIGURE 4.11: (a) Infrared image of TJ-II inner vessel immediately after a beam shot. The image is right-left inverted b) Photograph of TJ-II inner vessel as seen from NBI-1 beam duct.

The transmitted power in a pulse with B field,  $P_{trans.}$  is given by

$$P_{trans.} = \frac{P_{neut.}}{P_{neut.+ions}} = \frac{\Delta T_B(\vec{B})}{\Delta T_B(no\vec{B})} < 1, \quad (4.20)$$

where  $\Delta T_B(\vec{B})$  is the temperature rise with  $\vec{B}$ -field ON and  $\Delta T_B(no\vec{B})$  is the temperature rise with  $\vec{B}$ -field OFF. The re-ionization rate is obtained as:

$$F_r = 1 - P_{trans.}. \quad (4.21)$$

In this study, the temperature rise at the profile maximum has been used. This leads to an estimate of the re-ionization ratio in the region of the beam axis. However, when the temperature profiles with and without  $\vec{B}$ -field are plotted, it is found that the re-ionization is not uniform in the beam cross section. This effect is seen for all beam parameters in the perveance scan, the re-ionization rate is lower in the region to the left of the beam. The most plausible cause is residual gas pressure inhomogeneity due to local gas re-emission sources.

Perveance scans in this case are done with/without TJ-II magnetic ( $\vec{B}$ -field). Changes in the temperature profile (maximum) at the BS with perveance are studied. The re-ionization profiles are obtained for a range of beam parameters.

## 4.7 Fast Ion Gauge (FIG)

Fast Ion Gauges (FIG's) have been used in previous studies to monitor the pressure rise at the beam duct during neutral beam injection. The large pressure surges observed in the duct have been associated to the gas locally generated

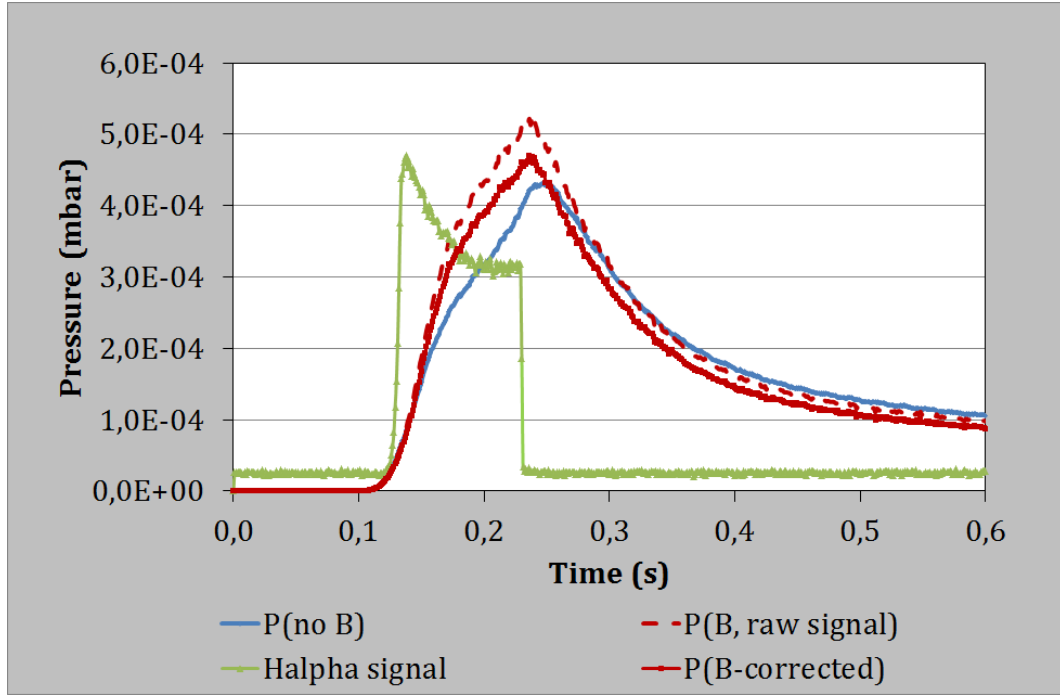


FIGURE 4.12: Time traces of the FIG signal for two injected beams: one with TJ-II  $\vec{B}$ -field OFF (blue line trace), and the other with TJ-II  $\vec{B}$ -field ON (red line traces). In the B-field case the two traces- raw signal and corrected signal- are shown. The Halpha trace (in green) is also shown, which shows the instants when the pulse is ON and OFF.

by the beam's impact on the duct walls [10]. For this study, the old Bayard-Alpert gauges have been substituted with Penning gauges, a great advantage when magnetic fields are present.

But even for the Penning gauges, the proximity of the gauge to the stellarator makes it prone to magnetic field perturbations. The  $\vec{B}$ -field effects need to be taken into account/compensated in the measurements. By performing gas pulses with/without  $\vec{B}$ -field the correction factor is found. In Fig. 4.12 the pressure traces corresponding to two injected beam pulses (without plasma) are shown. The beam parameters are the same but one of the pulses is performed in the presence of TJ-II  $\vec{B}$ -field, while the other is injected without  $\vec{B}$ -field. For the  $\vec{B}$ -field case two traces are shown: the raw Penning gauge signal and the corrected trace with the 0.9 factor. In the analysis of the Beam Stop pulses, the pressure traces for pulses with TJ-II B field have been normalized by the 0.9 factor.

In Fig. 4.12, it is observed that the pressure rise is higher in the case with  $\vec{B}$ -field. It means that the vessel wall areas stricken by the re-ionized particles are less well conditioned than the direct impact areas, therefore a higher gas re-emission comes from these regions.

The reaction rate of beam particle re-ionization is proportional to the product of the population of reactants (fast neutrals and thermal gas molecules), there-

fore higher re-ionization rates are expected in pulses with greater pressure rise. In the perveance scans carried out in this study, the pressure rise is monitored, and a relationship between re-ionization rate and pressure rise is sought.



# Chapter 5

## Results

### 5.1 V-calorimeter

In the V-Calorimeter, the full beam is intercepted. Therefore, the power transmission is obtained as the ratio of the power that reaches the calorimeter to the ion beam power at the Ion Source (*Pelec*). *Vaccel* and *Iaccel* scans have been performed, and for each set of beam parameters the beam transmission, neutralization fraction and perveance plot have been obtained.

Tab. 5.1 and 5.2 present the current and energy scans carried out on the V-calorimeter. The same parameter scans have been carried out in the TC and BS experiments. The beam current scans were realized by varying *Iaccel* at constant *Vaccel* while in the energy scans *Vaccel* is varied at constant *Iaccel*. The aim is to keep one of the two beam parameters constant while varying the other, but slight variations in the constant parameter are unavoidable due to the behavior of the high voltage power supplies. Pulses with Bending Magnet (BM) ON and OFF were performed for each set of beam parameters, to obtain the Beam Transmission and Neutralization Fraction. In the tables, the perveance is expressed in  $\mu\text{Perv.} = 1 \times 10^{-6} \text{ AV}^{-3/2}$ , the transmission (Trans.) and neutralization fraction (Neutr. Frac) are also shown.

Fig. 5.1 and 5.2 summarize the results of the current and energy scans on the V-calorimeter. The ion source power (*Pelec*) and the power delivered to the V-calorimeter with (BM)/without (NoBM) bending magnets, the neutralization fraction and the transmitted power dependencies on *Vaccel* and *Iaccel* are shown. The power transmission dependencies on the micropervance ( $\mu\text{Pervance}$ ) for the two cases are also shown. The beam perveance is calculated using the relation in Eq. 2.6.

In Fig. 5.1a., a linear dependency of the ion source power (*Pelec*) on the beam current is shown; the slope of the straight line is the beam voltage. The power transmitted to the calorimeter without the bending magnet (NoBM) is a fraction of the power supplied in the ion source due to geometrical transmission losses (beam divergence) and losses in the Grids. With BM ON, the non-neutralized fraction does not reach the calorimeter.

<i>Iaccel</i>	<i>Uaccel</i>	<i>Pvcal</i>	<i>Pelec</i>	$\mu$ Perv.	<i>Pvcal</i>	<i>Pelec</i>	$\mu$ Perv.	<i>Tr.</i>	<i>N.F</i>
(A)	(kV)	(kW)	(kW)	(AV <sup>-3/2</sup> )	(kW)	(kW)	(AV <sup>-3/2</sup> )	(%)	(%)
61.3	31.5	1039	1900	10.793	1588	1906	10.809	83	65
59.1	31.9	1020	1852	10.185	1567	1848	10.138	85	65
57.1	32.2	1001	1798	9.634	1544	1797	9.615	86	65
55.3	31.0	944	1683	9.937	1417	1683	9.926	84	67
53.9	31.3	919	1644	9.487	1394	1639	9.472	85	66
52.6	31.5	926	1609	9.166	1366	1603	9.122	85	68
48.8	32.0	826	1514	8.306	1253	1509	8.285	83	66
45.9	32.3	780	1435	7.672	1181	1438	7.698	82	66
45.6	30.9	765	1368	8.166	1131	1365	8.172	83	68
43.7	31.1	739	1308	7.691	1086	1311	7.700	83	68
40.9	31.4	694	1227	7.035	984	1233	7.081	80	71

TABLE 5.1: *Iaccel* scan results. On the left hand side are listed the cases “with” Bending Magnet ON, and to the right are the cases “without” BM. The Neutr. Frac is denoted by *N.F* and Trans. by *Tr.*.

<i>Iaccel</i>	<i>Uaccel</i>	<i>Pvcal</i>	<i>Pelec</i>	$\mu$ Perv.	<i>Pvcal</i>	<i>Pelec</i>	$\mu$ Perv.	<i>Tr.</i>	<i>N.F</i>
(A)	(kV)	(kW)	(kW)	(AV <sup>-3/2</sup> )	(kW)	(kW)	(AV <sup>-3/2</sup> )	(%)	(%)
52.7	25.5	710	1310	12.628	970	1317	12.627	83	65
52.6	27.0	776	1852	11.629	1107	1396	11.667	85	65
52.8	28.5	840	1394	10.784	1223	1473	10.783	86	65
53.0	29.9	883	1555	10.102	1300	1553	10.075	84	67
53.4	31.3	906	1635	9.440	1364	1634	9.433	85	66
53.4	32.6	936	1715	8.855	1445	1727	8.932	85	68
53.7	34.1	954	1804	8.395	1509	1798	8.376	83	66

TABLE 5.2: Energy scan results. On the left hand side of the table are listed the cases “with” Bending Magnet ON, and to the right are the cases “without” BM. The Neutr. Frac is denoted by *N.F* and Trans. by *Tr.*.

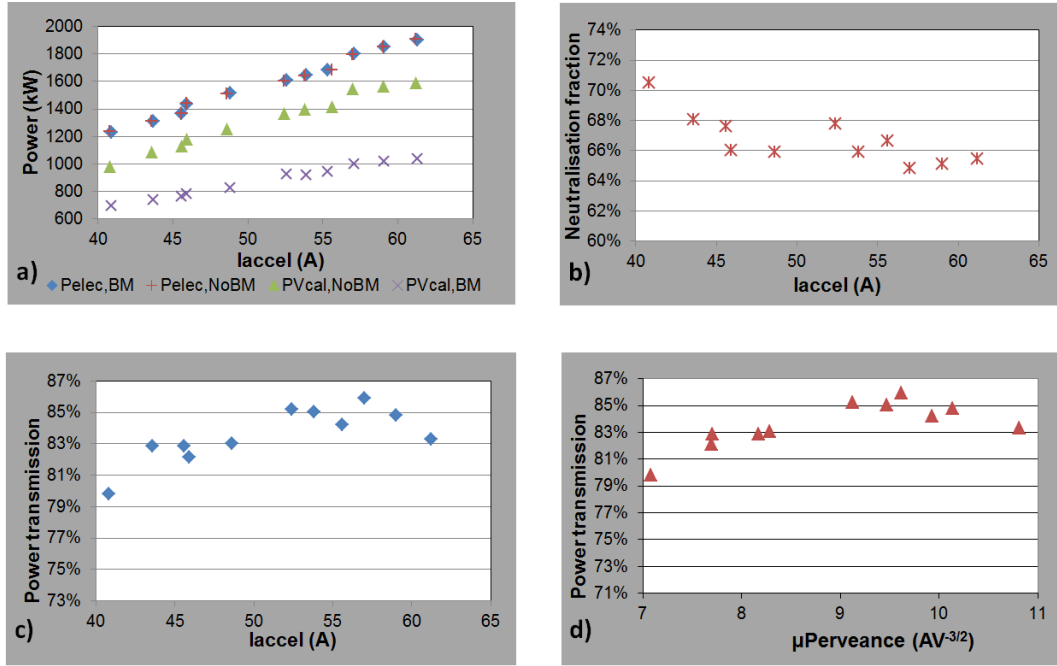


FIGURE 5.1: Beam current scans on V-calorimeter. a) Power in the ion source (*Pelec*) and power on the calorimeter with and without bending magnets functions of acceleration current ( $I_{accel}$ ). b) Neutral beam-power fraction as a function of  $I_{accel}$ . c) and d) show the beam transmission as a function of  $I_{accel}$  and perveance respectively.

The neutralization fraction slightly decreases with increasing current even though the beam energy is kept constant. Since the neutralization cross section depends only on the fast ion energy, the expectation is that the neutralization fraction should not vary with  $I_{accel}$ .

However, the  $I_{accel}$  scan is achieved by varying the arc Voltage  $V_{Arc}$ , which is known to influence the molecular ion ratios in the ion source. For increasing  $V_{Arc}$ , the  $H^+$  species is favored, therefore the average beam energy increases for increasing  $I_{accel}$ .

Beam transmission increases and maximum transmission is achieved for values of beam current around 55 A, and the corresponding beam perveance between 9.0 and 10.8  $\mu AV^{-3/2}$ . Below and above optimum perveance, the beam transmission decreases.

Fig. 5.2 shows the results of the beam energy scans on the V-calorimeter. In a) the ion source power (*Pelec*) increases linearly with energy (the slope is the constant  $I_{accel}$ ). The power transmitted to the calorimeter with BM OFF is less than the supplied power, due to beam divergence (geometrical) and Ion Source (Grids) losses. With the bending magnet ON, the power on the calorimeter is a lower fraction of the power in the ion source, since a considerable amount of power is lost with the un-neutralized ions to the ion dump. The beam power transmission increases for energies between 25 keV

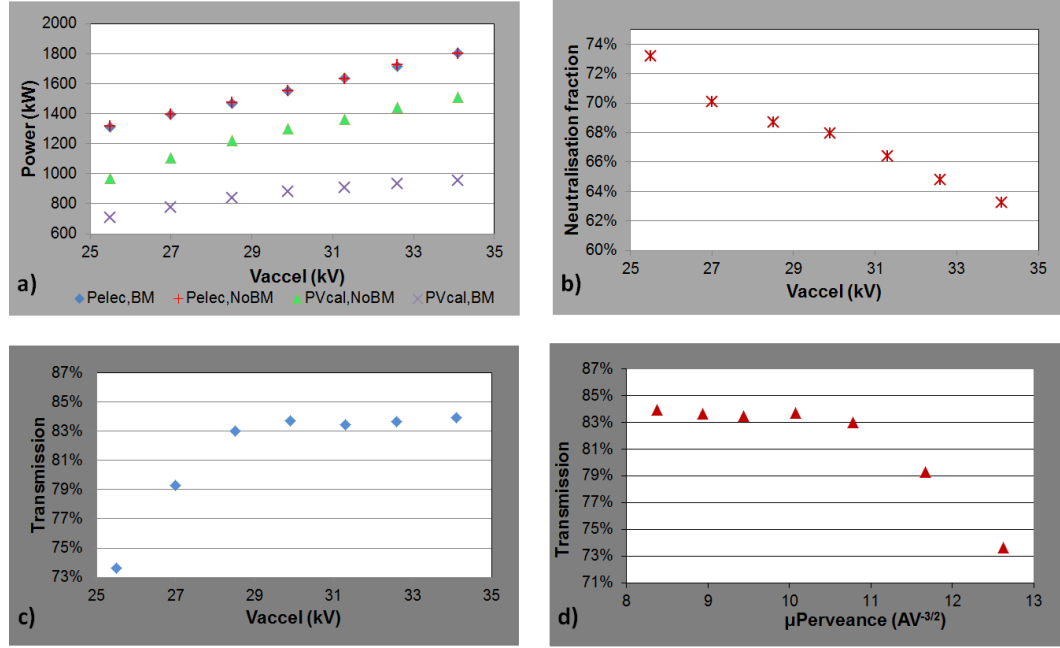


FIGURE 5.2: Beam energy scans on the V-calorimeter. a) Power in the ion source (*Pelec*) and power on the V-calorimeter (*Pcal*) with (BM) and without (NoBM) as functions of beam energy (*Vaccel*). b) Neutralization fraction as a function of beam energy. Beam power transmission as a function of c) beam energy and d)perveance.

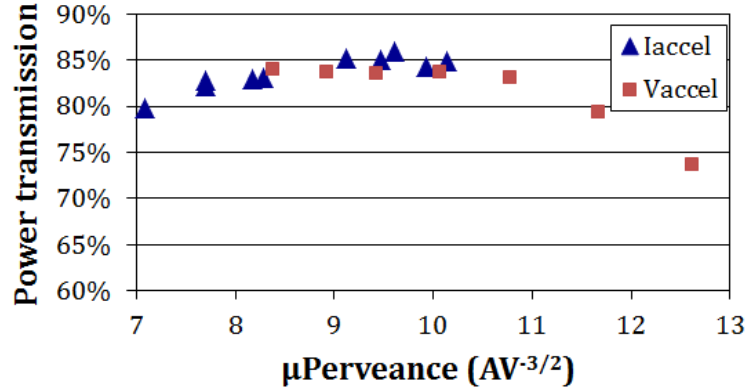


FIGURE 5.3: The transmission results of the Iaccel and Vaccel scans are plotted as a function of Perveance.

and 29 keV, and then becomes constant in the range considered. Maximum transmission is about 84 %, and is achieved for a range of values of the beam perveance, which correspond to the optimum perveance values (8.3–11.1  $\mu AV^{-3/2}$ ) for the given grid geometry. Above the optimum perveance, the beam transmission decreases.

In Fig. 5.3 the results of the two scans are represented on the same plot. Although the ranges of perveance in the two scans are different, the two transmission curves merge in the overlapping interval. This result illustrates the



expected behavior of the ion extraction system - that the transmitted ion current depends mainly on beam perveance, as corresponds to a space-charge limited extraction system.

There is an observed difference in the beam transmission between the two scans; the transmission is more peaked for current perveance scans whereas it is flatter for the energy scans. This difference can be explained by the way in which the *Iaccel* scan is performed: by scanning the Arc voltage, differences in molecular ion mix appear, which translate into differences in transmission since molecular ions have different trajectories in the electric field of the accelerating system.

In the perveance expression for a single beamlet (Eq. 2.6), it is seen that the optimum perveance value depends on the charge to mass ratio  $Z/M$ , which is a critical parameter in determining the ion trajectories. For real beams with energy species mix, this dependence is averaged out between the three ion species ( $H^+$ ,  $H^{2+}$ , and  $H^{3+}$ ). In the beam current scans described here, the relative abundance of full energy ions  $H^+$  (30 keV) increases as *Iaccel* increases, and therefore the optimum perveance value changes along the curve in (d). The current scan is not a pure perveance scan, therefore the observed differences.

## 5.2 Target Calorimeter (TC)

The Target Calorimeter (TC) intercepts the full beam power after the beam duct, at a location near the beam focus. The beam power distribution is therefore expected to approach a Gaussian. Infrared thermography of the TC after the beam pulse is used to obtain the power density profiles, which, when fitted to a single Gaussian yield the  $1/e$  beam divergence angle. Beam Energy and Current scans have been performed, and the divergence angle is obtained for each set of beam parameters. The dependence of beam divergence on perveance is sought.

Fig. 5.4 and 5.5 respectively show the beam current and beam energy scan results for the horizontal (a) and vertical (b) temperature increment ( $\Delta T$ ) profiles in Image Coordinates as obtained by Infrared thermography of the Target Calorimeter.

The highest value of the peak in  $\Delta T$  is  $33.6^\circ\text{C}$  at 34 keV energy and  $8.4\mu\text{Perv}$  for the energy scan and  $33.4^\circ\text{C}$  for a beam current of 53.6 A and  $9.1\mu\text{Perv}$ .

For the current scan, the peak  $\Delta T$  increases for increasing currents from 40.6 A to 53.6 A and remains almost constant. It then decreases for currents above 57 A in the considered range. The *Iaccel* values corresponding to the highest values of the peak  $\Delta T$  correspond to the optimum perveance values obtained in the V-calorimeter scans.

For perveance values above the optimum, the power transmission (V-Cal) and peak power density (TC) decrease in spite of having greater beam power.

Scans in beam energy show an increase of the peak  $\Delta T$  for increasing

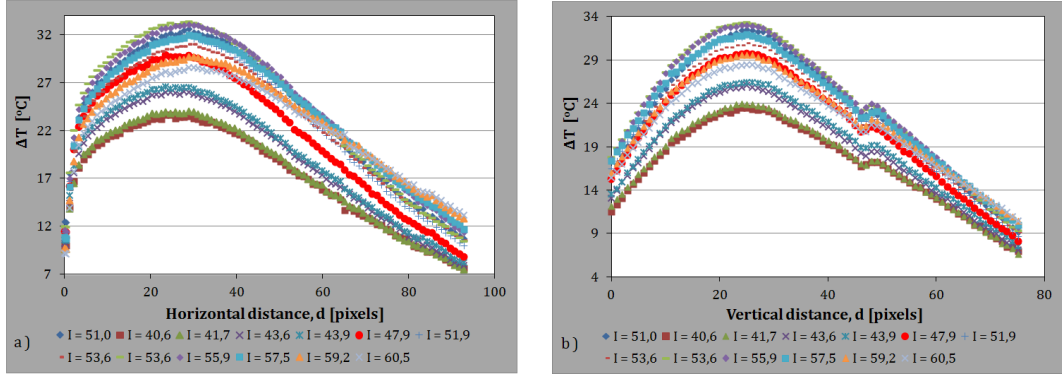


FIGURE 5.4: Beam current ( $I_{accel}$ ) scan  $\Delta T$  profiles in Image coordinates. a) Horizontal profiles and, b) Vertical profiles for different  $I_{accel}$ , given by  $I$  (A).

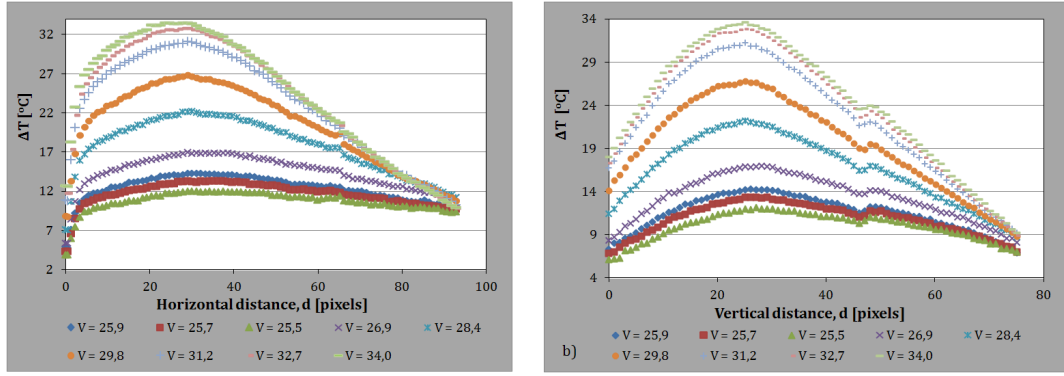


FIGURE 5.5: Beam energy ( $V_{accel}$ ) scans: Horizontal (a) and vertical (b) temperature profiles in Image coordinates for varying  $V_{accel}$ , given by  $V$  (kV).

extraction voltages, for all the range of  $V_{accel}$  variation, following the increase in the beam power. Perveance changes do not affect this trend.

In the Image Coordinate profiles, the abscissae correspond to the distance, in pixels, to a common origin, chosen to the left of the beam. In this way, the left-right inversion of the image is corrected, and the profiles in both coordinate systems (IC and BC) can be easily compared. A sharp boundary is observed on the left hand side (LHS) of the horizontal temperature profiles in Image coordinates (Fig. 5.4a. and 5.5a.). The depletion in power density is due to the scraping of the beam by the left wall of the port. In Fig. 5.6, a cross section of the injection port is shown, with the beam axis intersection. By design, the beam axis is not centred in the port. The injection direction was chosen after a careful optimization process, where the overall beam efficiency, including beam-plasma power coupling, was considered. The scraping effect of the port is consequently more pronounced to the left of the beam. No beam scraping is observed in the vertical profiles.

In both horizontal profiles of Fig. 5.4a. and Fig. 5.5a., the peaks of  $\Delta T$  (which correspond to the beam centre) are seen to slightly shift in position as the beam parameters are changed. This effect may be caused by misalignments

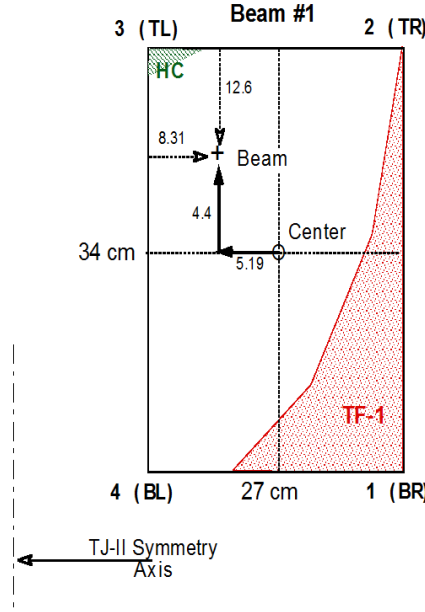


FIGURE 5.6: Cross section of the beam duct at the injection port, as seen from the beam direction. At the top-left corner, the vacuum vessel ‘groove’ where the CC coils are housed is shown. At the bottom-right the contour of the TF-1 coil is represented.

at the grids that affect the focusing and power distribution of the beam.

For the vertical profiles, the results are affected by the viewing window which limits the field of view in the vertical direction. The temperature is significantly undervalued at the profile tails, corresponding to viewing angles grazing the window edges. This shows dramatically in the comparison between the two copper buttons, which is the reason why the vertical profiles have been discarded in this study. In the following, the analysis will be restricted to the horizontal profiles.

Fig. 5.7 shows the horizontal temperature profiles in Beamline coordinates for the current (a) and energy (b) scans. Negative values of the Horizontal coordinate  $X$  are on the right as corresponds to the definition of Beam coordinate system.

The temperature profiles in Beam coordinates are not centred at  $X = 0$  as should correspond to the nominal beam direction (remember the definition of the beam coordinate system, Tab. 4.6) but rather they appear shifted by 2.0 cm to the left. This shift is due to a change in beam steering by  $0.25^\circ$  that has been the working position for the beam during the present experimental campaign.

From the relation in Eq. 4.18, the graphite temperature ( $\Delta T_g$ ) values can be changed into the power density perpendicular to the beam, and a power density profile obtained.

Fig. 5.8 shows the temperature profiles in Fig. 5.7 translated into power density

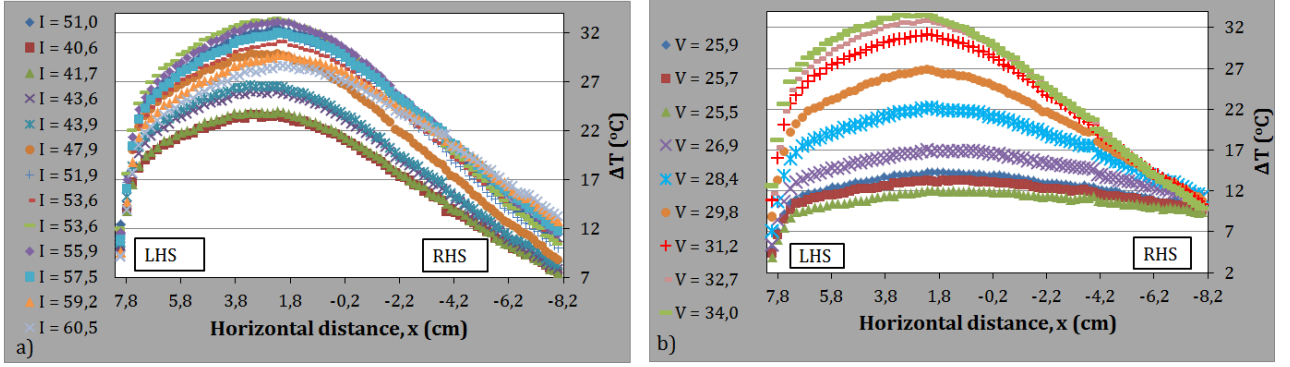


FIGURE 5.7: Horizontal profiles for the current (a), and energy (b) scans, in Beam-line coordinates.

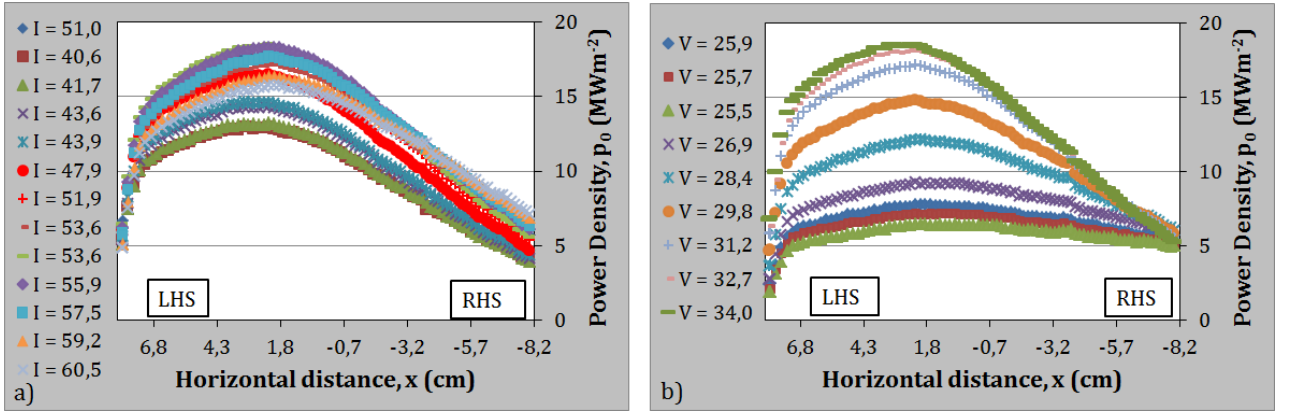


FIGURE 5.8: Horizontal beam power density profiles for the current (a), and energy (b) scans, in Beamline coordinates.

profiles

The power density profiles were fitted to a Gaussian of the form in Eq. 2.7 to estimate the beam divergence. As an example the Gaussian fits for two horizontal profiles corresponding to beams of similar parameters are shown in Fig. 5.9.

From the Gaussian fits, the  $1/e$  widths (a) were determined in each case, and the corresponding  $1/e$  divergence angle,  $\theta_{1/e}$ , estimated from:  $a = d \cdot \tan \theta_{1/e}$ , where  $d = 4,541.5$  mm is the distance between Ion Source and TC.

In Fig. 5.10, the horizontal  $1/e$  divergence and the beam transmission dependencies on the beam perveance are shown for the current scans (a) and energy scans (b).

In both scans, maximum transmission occurs when the  $1/e$  divergence angle is minimum and almost constant. Below or above the optimum perveance, the  $1/e$  divergence increases. This is in total agreement with the definition of perveance.

In Fig. 5.11 the divergence half-angle is plotted as a function of perveance for the two parameter scans. The merging of the two scans confirms that the

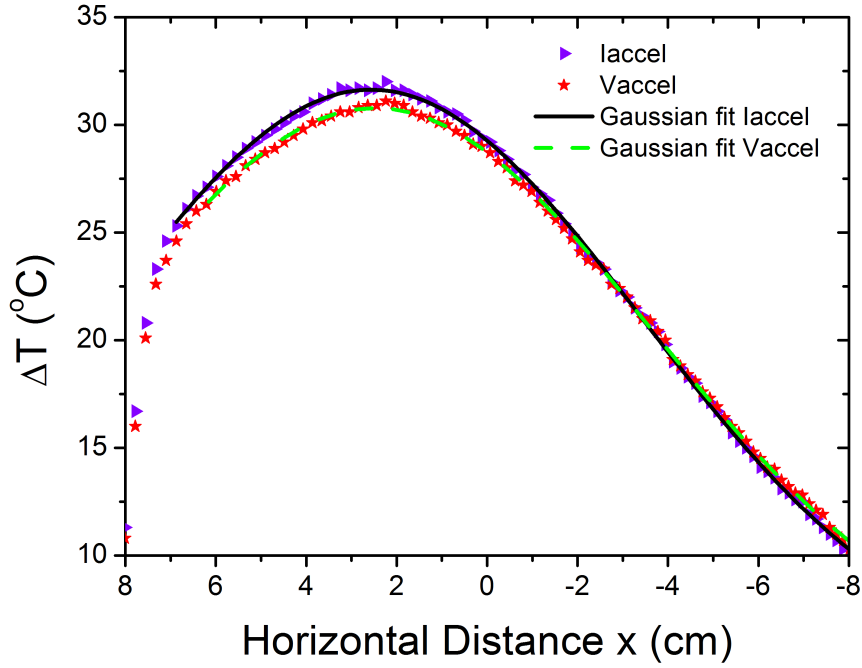


FIGURE 5.9: Gaussian-fitted curves for two beam profiles. *Iaccel* profile corresponds to  $I = 51.9$  A, and *Vaccel* is the  $V = 31.2$  kV case.

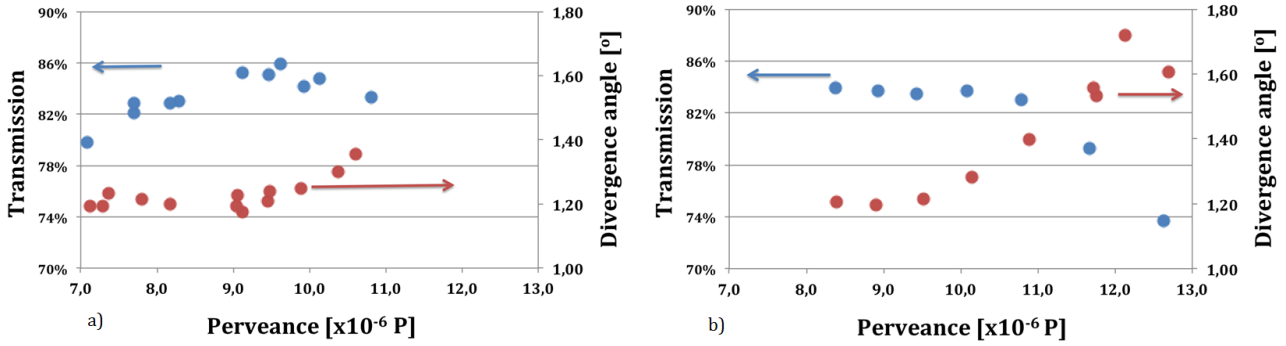


FIGURE 5.10: Horizontal  $1/e$  divergence half angle,  $\theta_{1/e}$ , and beam power transmission dependencies on beam perveance. a) Current scans b) Energy scans.

beam divergence depends solely of perveance, irrespective of the beam power.

### 5.3 Beam Stop (BS)

A series of beam pulses were launched onto TJ-II vacuum chamber in the absence of plasma, to study the reionization losses for beam parameters spanning a wide range of beam energy (*Vaccel*) and beam current (*Iaccel*) values.

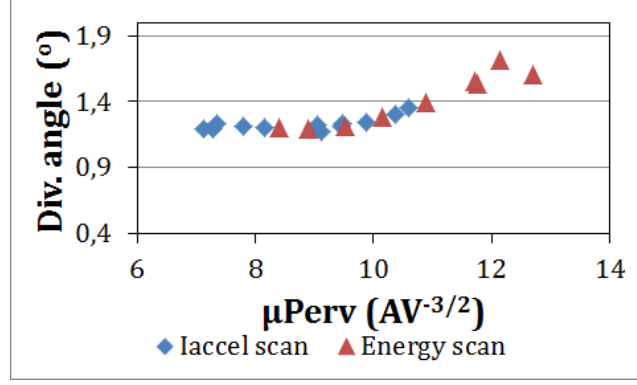


FIGURE 5.11: Horizontal  $1/e$  divergence half angles,  $\theta_{1/e}$ , as a function of perveance.  
a) Current scans b) Energy scans.

Beam injection in the absence of plasma does not pose any risk associated to the elevated thermal loads, as has been shown with Beam simulation studies using a detailed 3D model for TJ-II vacuum chamber [25]. Due to the short pulse length ( $< 200$  ms), the chamber wall temperature does not attain critical values at any of the interaction surfaces. The main fraction of beam power is deposited on the Beam Stop (60 %) with lesser fractions on the Hard Core (14 %) and TF protection (20 %). As in the previous experiments/targets, two different parameter scans were performed: a beam current scan ( $47 \text{ A} < I_{\text{accel}} < 60 \text{ A}$ ) and a beam energy scan ( $26 \text{ kV} < V_{\text{accel}} < 34 \text{ kV}$ ).

For each set of parameters, two pulses were performed: one without magnetic field, and one with TJ-II magnetic field (TJ-II coil currents for a standard configuration), to obtain the reionization fraction.

Fig. 5.12 and 5.13 respectively show current scan and energy scan results for temperature rise ( $\Delta T_B$ ) measurements on the Beam Stop target measured by IR thermography. The  $\Delta T_B$  dependencies on  $I_{\text{accel}}$  (5.12) and  $V_{\text{accel}}$  (5.13), and on the beam perveance are shown in (a) and (b). When  $\Delta T_B$  measurements are taken with TJ-II  $\vec{B}$ -field OFF, the full beam from the duct impinges on the Beam Stop target. The observed  $\Delta T_B$  therefore represents the full power of the beam from the duct.

With TJ-II  $\vec{B}$ -field ON, both scans show a reduction in  $\Delta T_B$ , since the beam power that reaches the beam Stop is reduced.

The  $\Delta T_B$  has the same dependence on  $I_{\text{accel}}$  and beam perveance for the two cases (B, NoB) and it is the same dependence as the transmission measured at V-Calorimeter.

In the same way, the observed dependence of  $\Delta T_B$  on  $V_{\text{accel}}$  and beam perveance is similar in the cases with and without the  $\vec{B}$ -field, but the  $\Delta T_B$  increases much faster with energy for no  $\vec{B}$ -field than with  $\vec{B}$ -field.

Fig. 5.14 and 5.15, respectively, show current scan and energy scan results for the beam re-ionization and the Fast Ion Gauge (FIG) measurements of the pressure build up at the duct exit. The plotted pressure corresponds to pulses with  $\vec{B}$ -field, since those are the pulses used to estimate the reionization

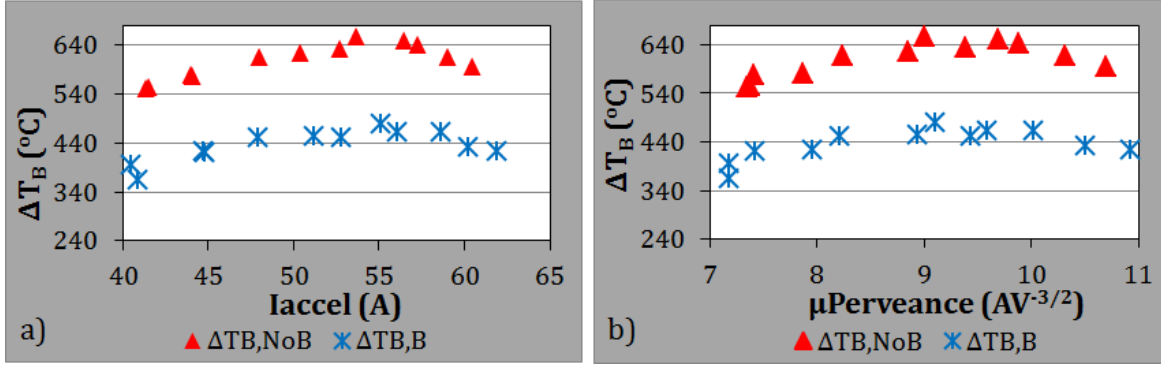


FIGURE 5.12: Beam Stop current scans: Temperature rise at the maximum,  $\Delta T_B$ , as a function of beam current (a), and perveance (b). The results are shown for TJ-II  $\vec{B}$ -field ON and for TJ-II  $\vec{B}$ -field OFF.

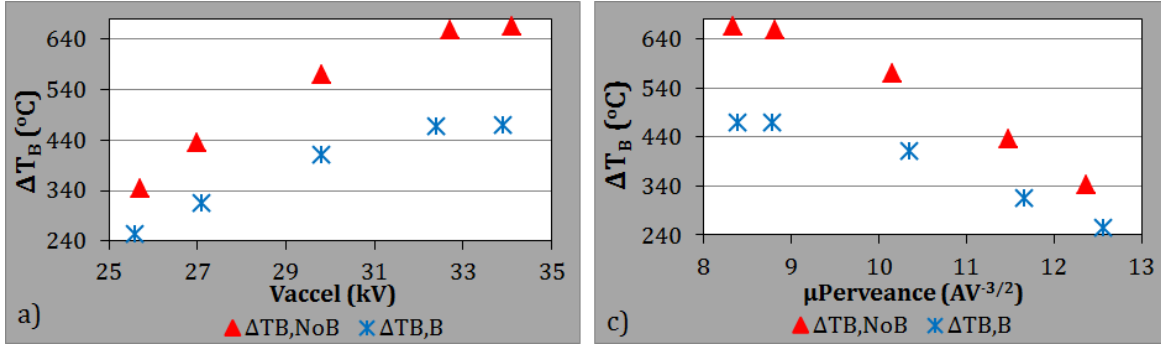


FIGURE 5.13: Beam Stop energy scans. (a) and (b) respectively show temperature rise,  $\Delta T_B$ , as a function of the acceleration voltage and beam perveance, for TJ-II  $\vec{B}$ -field ON and TJ-II  $\vec{B}$ -field OFF.

fraction. A 0.9 correction factor is applied to account for the  $\vec{B}$ -field influence on pressure readings of the Penning gauge. For each  $V_{\text{accel}}$  (or  $I_{\text{accel}}$ ) value, the ratio of  $\Delta T_B$  (max) for the  $\vec{B}$ -field case to the no  $\vec{B}$ -field case is represented. This ratio represents the transmission.

Fig. 5.14a. shows the pressure rise dependence on the beam current ( $I_{\text{accel}}$ ). The pressure is weakly dependent on  $I_{\text{accel}}$ . This result is intriguing and presents an interesting conundrum which deserves further investigation, since the pressure (due to gas re-emission) seems not related to beam power. As seen in Fig. 5.12a., the temperature excursion for the  $I_{\text{accel}}$  scan is smaller than in the  $V_{\text{accel}}$  scan, and so is the Pressure excursion, whereas the beam power excursion (at the V-Calorimeter) is larger. A clear conclusion cannot be drawn at this point, since the transmitted power must be calculated for the two scans with a beam simulation code, to take into account the variation in divergence. Low energy, low power beams of perveance over  $11 \mu\text{Perv}$  have high divergence angle ( $1.60^\circ$ ), therefore the number of injected particles can be significantly lower than the low power beams in the  $I_{\text{accel}}$  scan, where the divergence angle is only  $1.30^\circ$ .

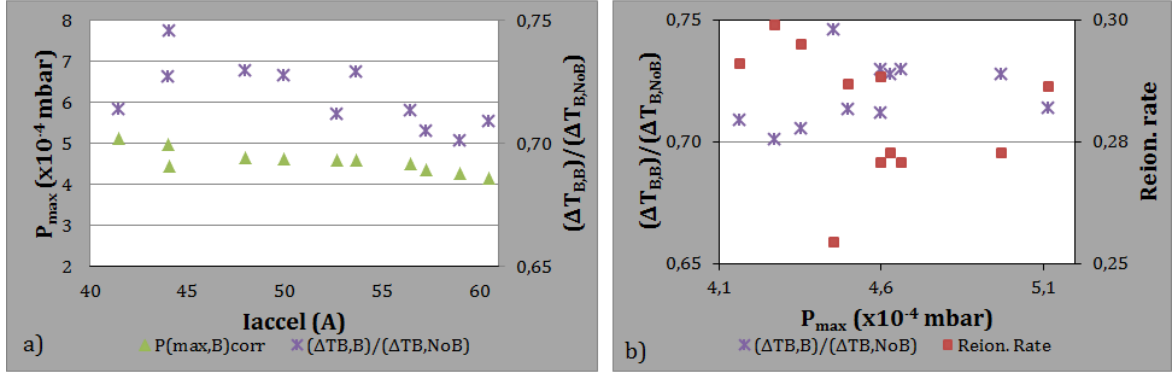


FIGURE 5.14: Current scan re-ionization rate (Reion. rate), transmission  $((\Delta T_B, B) / (\Delta T_B, NoB))$  and pressure ( $P_{max}$ ) measurements. a) FIG pressure measurements at the duct exit and transmission as functions of the beam current ( $I_{accel}$ ). b) Transmission and re-ionization rate as functions of duct pressure.

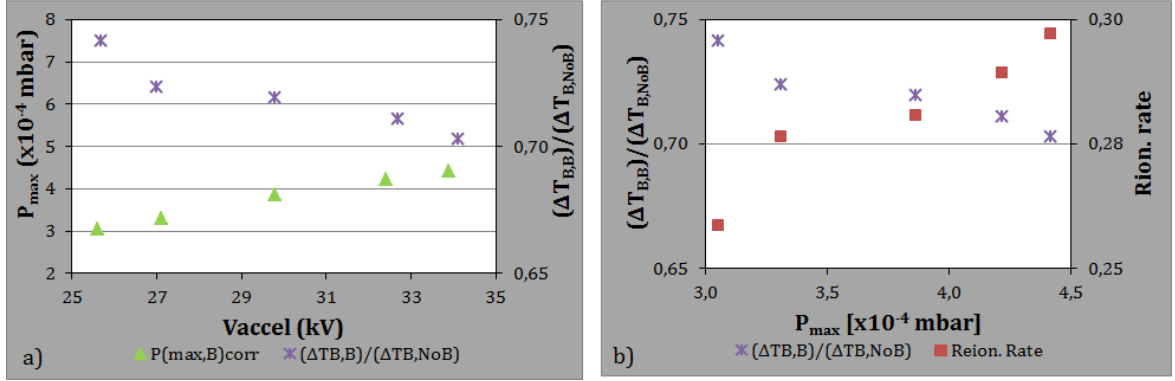


FIGURE 5.15: Energy scan re-ionization (Reion. rate), transmission  $((\Delta T_B, B) / (\Delta T_B, NoB))$  and pressure ( $P_{max}$ ) measurements. a) FIG pressure measurements at the duct exit and transmission as functions of the beam energy ( $V_{accel}$ ). b) Transmission and re-ionization rate as functions of the gas pressure build up at the duct exit.

A certain correlation is observed between transmission and  $I_{accel}$  in Fig. 5.14a.: the transmission decreases with  $I_{accel}$ . Since the increase in beam current is achieved by increasing  $V_{arc}$ , the increase in re-ionized fraction can be ascribed to the increase in population of full energy ions at the Ion Source, which have higher re-ionization cross section [9].

No correlation between transmission (re-ionization) and pressure is observed in the  $I_{accel}$  scan, as seen on Fig. 5.14b. But, according to Eq. 2.4, the reionized fraction should increase with the gas particle density (gas pressure), therefore, some competing effect, yet unknown, must be at the origin of this unexpected behaviour.

Fig. 5.15a. shows the pressure and transmission dependence on beam acceleration voltage, and Fig. 5.15b. shows the transmission and re-ionization



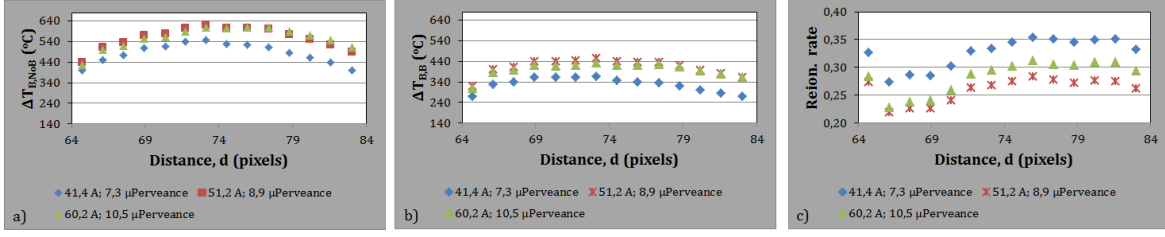


FIGURE 5.16: Current scans: a)  $\Delta T_B$  profile with TJ-II  $\vec{B}$ -field OFF. b)  $\Delta T_B$  profile with TJ-II  $\vec{B}$ -field. c) re-ionization rate across profile.

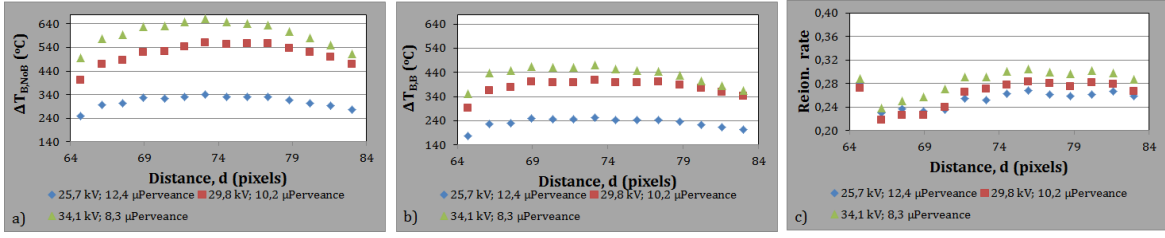


FIGURE 5.17: Energy scans: a)  $\Delta T_B$  profile with TJ-II  $\vec{B}$ -field OFF. b)  $\Delta T_B$  profile with TJ-II  $\vec{B}$ -field c) re-ionization rate across profile.

rate dependence on pressure.

The transmission decreases with  $V_{\text{accel}}$  whereas the pressure increases with  $V_{\text{accel}}$  (a). In (b) the re-ionization rate increases with pressure. The decrease in transmission (increase of reionization rate) with increasing  $V_{\text{accel}}$  is due to:

- The dependence of the re-ionization cross section on Energy:  $\sigma_{01}$  increases monotonously with energy up to 45 keV, where a maximum is found [9, 8].
- The increase in gas target thickness (Pressure) with  $V_{\text{accel}}$ : beam power increases linearly with  $V_{\text{accel}}$ , and so does the intercepted power on the solid surfaces, giving rise to increased gas re-emission.

In the quest for a more detailed understanding of the beam transmission and re-ionization in the vacuum chamber, we also explored their distribution around the beam centre (maximum temperature) in the beam cross section. Here, the  $\Delta T_B$  variation along a profile drawn on the Beam Stop is presented both for the pulses with, and without the TJ-II  $\vec{B}$ -field. The re-ionization rate across the profile is shown in Fig. 5.16c. and 5.17c.

The profiles are studied for three sets of  $I_{\text{accel}}$  and  $V_{\text{accel}}$  values, ensuring a good span of beam perveance values including the optimum.

Results for the current scan are shown in Fig. 5.16 while Fig. 5.17 shows the results from the energy scans.

In the  $I_{\text{accel}}$  scan, three temperature profiles for three  $I_{\text{accel}}$  values are shown. An asymmetry is found in the re-ionization profile for the three  $I_{\text{accel}}$  values.

Temperature rise on the Beam Stop ( $\Delta T_B$ ) and re-ionization rates along a profile for three different beam energies are shown in Fig. 5.17) (a-c) . The 8.3 and 10.2  $\mu$ Perveance values are optimum perveance values, whereas 12.4  $\mu$ Perveance is above optimum.

The re-ionization rate profile has a depletion area to the left of the beam. This result appears for the three beam energies considered. The low reionization area seems a consistent effect that can only be interpreted as due to a local minimum in the gas target thickness.

# Chapter 6

## Discussion

Beam transmission has been studied for a range of beam parameters corresponding to two different scans: a beam current scan at constant beam energy, and a beam energy scan at constant beam current. In the scans, the beam perveance is varied together with beam power, and consequently the optical properties of the beam are changed. It is important to determine the beam geometrical transmission when scanning the beam parameters during plasma experiments, since the number of injected fast particles is relevant in the study of such phenomena as the excitation of Alfvén waves in the plasma or the power threshold for the transition to high confinement mode ('H' mode).

Also, the power losses due to reionization may deplete beam power and fast particle current, affecting the beam power balance.

In this study, the transmission of the beam has been studied at three targets along the beam path:

- The V-calorimeter that intercepts the full beam upstream of the beam duct, allows to obtain the beam transmission and neutralization fraction. The dependence of transmission on perveance has been determined for the parameter scan of this study. But it does not take into account the beam losses at the duct and TJ-II entrance, that can be important. Nor does it give information on the power density profile, that would allow to calculate the transmission with a beam simulation code.
- The Target Calorimeter (TC) allows to obtain power density profiles of the beam at the duct exit, near the beam focus. From the Gaussian fits of the profiles, the beam angular divergence can be extracted. Using a Gaussian model for the beam, the power transmission can be simulated with a computer code, from which the power and particle transmission to the plasma can be obtained. This simulation lies outside the scope of this thesis, but will be the object of a future study based on the divergence values reported in this work.

For the parameter scans in this study, the perveance value that leads to maximum transmission at the V-calorimeter, corresponds to minimum divergence and maximum temperature at the Target Calorimeter.

Temperature readings with an infrared camera are prone to large uncertainties related to the changing emissivity of surfaces, or the influence of the optical alignment. Two copper calorimeters with embedded thermocouples allow an independent calibration of the temperature map by assigning a known power density with a given isotherm. The temperature profiles are therefore converted to power density profiles.

The infrared thermography at the TC allows the determination of the beam center location, it has proved a reliable way to measure the beam steering.

But further reduction of the beam power is produced by the re-ionization reactions of the fast neutrals with the molecules of the residual gas present in the vacuum chamber. In order to estimate the re-ionization losses, infrared thermography is used to obtain thermal images of the Beam Stop.

- **Beam Stop:** In the beam parameter scans performed, the maximum temperature increments on the BS correspond to optimum perveance. Comparison of the target temperatures in shots with/without  $\vec{B}$ -field, yields an estimate of the re-ionization fraction.

Re-ionization has been estimated for the same beam parameter scans as for the other targets. In the present experiments large re-ionization fractions (25 %–35 %) in excess of the more usual values (15 %–20 %) have been found. A good correlation between re-ionization losses and residual gas pressure is found for the beam energy scans, but not for the current scans. It remains a riddle to be solved in the future that there is little or no variation in pressure during a beam current scan. Re-ionization profiles have been obtained at the BS target, showing a clear valley to the left of the beam axis. It remains as a future task to determine the consistency of this finding and compare these profiles with those obtained for the second NBI.

# Chapter 7

## Summary

From the measurements at the three different targets, we have been able to experimentally:

1. measure the power transmission and neutralization fraction at the V-calorimeter as functions of beam extraction energy, beam current and beam perveance.
2. measure the horizontal and vertical temperature profiles along the beam cross section on the Target Calorimeter for energy and current scans.
3. estimate the beam's horizontal power density profile on Target Calorimeter (along beam cross section) using temperature measurements on two adiabatic calorimeters coplanar with the TC plates.
4. estimate the beam's horizontal  $1/e$  divergence angles.
5. study the dependence of gas pressure build up at the duct exit on beam energy and beam current.
6. study the dependence of re-ionization rate and beam power transmission on gas pressure build up in the duct exit.
7. determine the re-ionization profile at the beam stop to study possible asymmetries.

These tools provide the necessary input for the simulation code that will allow for the estimate of the true beam power and fast particle contribution to the plasma energy and particle balance.



# Chapter 8

## Appendix

### 8.1 Appendix 1

Tab. 4.6 shows coordinates of the  $T_{max}$  point on the TC and the two extreme points used for the construction of horizontal and vertical beam profiles in both their Image and Beamline co-ordinates.

Using the OPTRIS camera software, a line between the two extreme points, passing through the maximum, was drawn. Since the image is right-left inverted, the point to the right of the image was taken as the start point for the horizontal profile, to ensure that the profile origin is to the left in the Target. Care was taken to have the line to the right of the image extended until it hits the image frame to ensure that the profile truncation due to beam interception by the injection port is seen.

When the saved thermographic files are loaded to the OPTRIS PI 160 camera software one at a time with the two lines drawn on the image, a file with the temperature profile data is generated and saved after the required image subtraction has been performed.

To draw the profiles in Image coordinates, distances “ $d$ ” (in non-integer pixel units) from a chosen origin were taken as horizontal axis for the temperature profiles. From the image shown in Fig. 8.2a., the reference (zero position) considered when measuring the vertical distances across the profile is below

	Image Co-ordinates (x, y)	Beam line Co-ordinates (X,Y,Z)
<i>Maximum Temperature position</i>	(132, 94)	(26.825, 4.295, 397.63)
<i>Horizontal extreme 1</i>	(160, 104)	(88.015, 4.295, 459.475)
<i>Horizontal extreme 2</i>	(71, 71)	(-78.675, 4.295, 291.002)
<i>Vertical extreme 1</i>	(134, 119)	(26.825, -41.422, 397.652)
<i>Vertical extreme 2</i>	(129, 43)	(26.825, 109.795, 397.58)

FIGURE 8.1: Image and Beamline coordinates used for generating the horizontal and vertical profiles through the position of maximum temperature (corresponding to the beam centre).

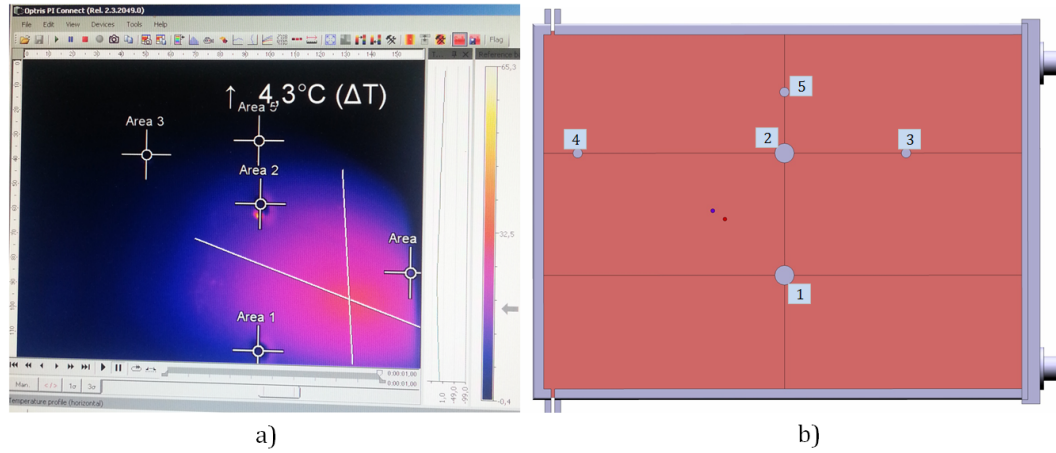


FIGURE 8.2: Left-Right inversion of TC IR image. a) IR image, with horizontal profile line drawn from right hand side of image. b) A Catia drawing of the TC. The button number labels in the Catia drawing correspond to the Area numeral labels on the IR image. It is not the case with the vertical profile.

the beam centre (near Area 1), while for the horizontal profiles it is to the right of the beam centre. The beam centre corresponds to the intersection of the two lines for the profiles shown in the Fig. 8.2a..

These profiles could not be used for determining the beam divergence since the spatial coordinates are heavily distorted due to the optical detection geometry. The Image coordinates had to be transformed to Beam Coordinates, using a matrix that describes the projective transformation. Since the angle between the target and the beam axis is  $45^{\circ}$ , the horizontal profiles were converted to perpendicular planes (Beamline coordinates) by taking the cosine of  $45^{\circ}$  (which is equivalent to taking the x coordinate in the Beam system).



# Bibliography

- [1] T. J. M. Boyd and J. Sanderson, *The Physics of Plasmas* (Cambridge University Press, New York, 2003), p. 431.
- [2] F. F. Chen, *An Indispensable Truth. How Fusion Power Can Save the Planet* (Springer, Los Angeles, 2011), p. 433.
- [3] J. R. M. Solís, Fusion Reactor Physics Lecture Notes, Fusion Master Erasmus Mundus, Universidad Carlos III de Madrid, Spain, 2013.
- [4] <http://iter.rma.ac.be/en/physics/how2doit/Magnetic/index.php>, ITER and Fusion Energy: Magnetic Confinement Fusion.
- [5] W. M. Stacey, *Fusion: An Introduction to the Physics and Technology of Magnetic Confinement Fusion* (Wiley VCH, Weinheim, Germany, 2010), p. 246.
- [6] M. Kikuchi, K. Lackner, and M. Q. Tran, *Fusion Physics* (IAEA, Vienna, Austria, 2012), p. 1129.
- [7] A. T. Forrester, *Large Ion Beams: Fundamentals of Generation and Propagation* (John Wiley and Sons, New York, 1988), p. 325.
- [8] E. Speth, Reports on Progress in Physics **52**, 57 (1989).
- [9] S. K. Allison, Rev. Mod. Phys. **30**, 1137 (1958).
- [10] M. Liniers *et al.*, Fusion Engineering and Design **88**, 960 (2013).
- [11] I. G. Brown, *The Physics and Technology of Ion Sources* (John Wiley Sons, Berkeley California, 1988), pp. 23–51.
- [12] I. G. Brown, *The Physics and Technology of Ion Sources* (Wiley-VCH, Weinheim, 2004), pp. 61–85.
- [13] J. Kim and J. H. Whealton, Nuclear Instruments and Methods **141**, 187 (1977).
- [14] T. Estrada *et al.*, Contrib. Plasma Phys. **50**, 501 (2010).
- [15] R. Jiménez-Gómez *et al.*, Nuclear Fusion **51**, 15 (2011).

- [16] M. A. V. Zeeland *et al.*, Nuclear Fusion **52**, 9 (2012).
- [17] K. Nagaoka *et al.*, Nuclear Fusion **53**, 6 (2013).
- [18] [http://fusionwiki.ciemat.es/fusionwiki/index.php/TJ II](http://fusionwiki.ciemat.es/fusionwiki/index.php/TJ_II).
- [19] C. Alejaldre and the TJ-II Team., Fusion Technology **17**, 131 (1990).
- [20] M. Liniers *et al.*, Fusion Technology **1**, 307 (1998).
- [21] M. Liniers *et al.*, Vacuum **67/3-4**, 379 (2002).
- [22] M. M. Menon, R. N. Morris, and P. H. Edmonds, *ATF Neutral Beam Injection System* (Proceedings of the 11th Symposium on Fusion Engineering, Austin, Texas, U.S.A., 1985), Vol. IEEE Pub. No. CH2251-7, pp. 1269–1272.
- [23] W. L. Gardner *et al.*, Rev. Sci. Instrum. **53**, 424 (1981).
- [24] J. Guasp, M. Liniers, C. Fuentes, and G. Barrera, Fusion Technology **35**, 32 (1999).
- [25] C. Fuentes, Ph.D. thesis, Ciemat, Madrid-Spain, 2007.
- [26] H. Carslaw and J. Jaeger, *Conduction of Heat in Solids*, 2nd ed. (Oxford Science Publications, Oxford, 1959).
- [27] R. L. Johnson *et al.*, *Design and Upgrades to the PLT Neutral Beam Injectors for use on PDX and ISX-B* (Proceedings of the 8th Symposium on Engineering Problems of Fusion Research, San Francisco, California, 1979), Vol. IEEE Pub. No. CH1441-5, p. 1375.
- [28] W. L. Gardner *et al.*, *The ORNL Prototype PDX Neutral Beam Injection System* (Proceedings of the 8th Symposium on Engineering Problems of Fusion Research, San Francisco, California, 1979), Vol. IEEE Pub. No. CH1441-5, p. 972.
- [29] C. Fuentes *et al.*, Fusion Eng. and Design **82**, 926 (2007).
- [30] C. Fuentes *et al.*, Review of Scientific Instruments **77**, (2006).
- [31] C. Fuentes *et al.*, Fusion Engineering and Design **74**, 249 (2005).
- [32] D. Ciric, H. Falter, P. Massmann, and K. Mellon, Fusion Technology **2**, 827 (1994).
- [33] G. Vereda, Private Communication.
- [34] J. Guasp, Private Communication.
- [35] M. Liniers *et al.*, *Ion Trajectory Calculation in TJ-II NBI Ducts* (Proceedings of the 40th EPS conference on Plasma Physics, Espoo, Finland, 2013), Vol. ECA 37D P1-137 ISBN 2-914771-84-3.

# Acknowledgements

Here I would like to thank those who have helped.

First, I would like to express my heart-felt appreciation to the the Erasmus Mundus Programme under which my entire course of studies was funded, and I am very grateful to my promoter, Prof. Ramón Solís and the Fusion-EP Consortium for the teaching and training they offered to me and for their continued support throughout the Master Course. I would like to convey my sincere gratitude to my thesis supervisor, Dr. Liniers Macarena, for her support and technical advice throughout this thesis project. I really enjoyed and benefitted a great deal working under her supervision. I cannot forget to thank the entire CIEMAT team, and in particular the NBI group, with whom I worked during the entire project. I feel very much indebted to J. Guasp who helped with the image transformations. Finally, I cannot forget to thank my beloved Mum, Dad and my siblings for their moral support and encouragement during the entire period of study. The list is very long and I cannot mention all names of those who helped, but I am very thankful to whoever helped in one way or the other to see that this thesis project is a success. ...



# Declaration in lieu of oath

Herewith I declare in lieu of oath that I have prepared this thesis exclusively with the help of my scientific teachers and the means quoted by them.

City, the

---

Julius Damba

# Copyright Agreement

I hereby grant the FUSION-EP consortium the non-exclusive right to publish this work.

I declare that this work is free of copyright claims of third parties.

City, the

---

Julius Damba